

Doctoral Dissertation

**Photo-cathode studies for High
Performance Linear Accelerator**

Lei Guo

Graduate School for Advanced Sciences of
Matters, Hiroshima University, Higashihiroshima,
Hiroshima 739-8530, Japan

Supervisor: Professor Masao Kuriki

07 2017

Contents

List of tables	3
List of figures	7
Abstract	8
Acknowledgments	9
1 Introduction	10
2 Photo cathode in modern accelerators	16
2.1 ERL	16
2.2 FEL	19
2.3 Linear Colliders	21
3 Photocathode	24
3.1 Metal cathode	24
3.2 CsK ₂ Sb photocathode	25
3.3 NEA-GaAs photocathode	27
4 Substrate dependence of CsK₂Sb cathode	31
4.1 Experimental Setup	31
4.2 Substrate surface treatment	36
4.3 Experimental Results	38
4.4 Discussion	44
5 Effect of Gas Adsorption on NEA GaAs	47
5.1 Experimental Setup	47
5.2 Experimental Results	48
5.3 Discussion	51
6 Summary	57

Appendix	65
A NEA GaAs as a polarized electron source	66
B Atomic arrangement model of unit cell	68

List of Tables

2.1	Electron beam parameter of ERL project [21][22][37]	18
2.2	Parameters of electron gun for ERL[21][22]	19
2.3	Parameters of the electron beam for LCLS[43]	20
2.4	Parameters of the electron beam for LCLS II.[44]	21
2.5	The electron beam parameters at the gun exit of ILC.[50]	23
4.1	The maximum QE of the CsK ₂ Sb photo-cathode on Mo(100), Mo(amorphous), Si(100), Si (111), and GaAs (100) substrates at 532 nm are summarized.	44
5.1	Mass to charge ratio and ion current of the major peaks of the mass spectrum by QMS with CO ₂ introduction. The rightest row shows the candidate molecule. The inside of the parenthesis is the mother molecule.	54
B.1	The maximum QE of the CsK ₂ Sb photo-cathode with ζ of CsK ₂ Sb(100) and CsK ₂ Sb(111) surface at 532 nm are summarized.	70

List of Figures

1.1	Livingston plot, in which the horizontal axis represents year and the vertical axis represents acceleration energy, indicating that the energy increased rapidly in time.[1]	10
2.1	An overview graphic of the ERL.[35].	17
2.2	The conceptual diagram of FEL.[42]	20
2.3	A schematic overview of ILC layout based on the accelerator design described in Technical Design Report.[47]	22
3.1	Schematic drawing of the photo-electron emission from the NEA GaAs cathode. Electron excited by laser to the conduction band is thermalized. Because the state of the conduction bottom has higher energy than that of the vacuum, electron can be emitted through the surface thin barrier. [20]	28
3.2	A schematic diagram of the electric dipole made by Cs vapor-deposited on the GaAs surface. Electric dipoles are formed on the GaAs surface, and the surface potential is lowered.	29
4.1	The picture of the evaporation chamber.This evaporation chamber is made from SUS 304 chemically polished on the inner surface. The vacuum was maintained with an ion pump (ULVAC PST-100 100 l/s pumping speed)[102] and NEG (Non Evaporative Getter , SAES Capacitorr-D400 480 l/s)[103] and was kept at UHV (a typical pressure was 1.0e-8Pa).	32
4.2	3D drawing of the CsK ₂ Sb evaporation chamber. Up to 3 cathode pucks can be stored in the chamber. The cathode can be transferred through the gate valve to another vacuum chamber (vacuum suitcase) for cathode transportation.	33
4.3	The drawing of the cathode puck. For each cathode puck, a 15 mm × 15 mm substrate is placed on a molybdenum base plate.	33

4.4	The picture of the cathode holder. Up to 3 cathode pucks can be set. The holder can be moved vertically to adjust the position for evaporation, photo-electron emission, and transfer.	34
4.5	Si(100) and GaAs(100) substrates. Si(100) and Si(111) wafers with a of $\leq 0.002 \Omega\text{cm}^{-1}$ and GaAs(100) p-type wafer are employed as the substrates.	34
4.6	The substrates mounted on the puck. The substrate is soldered on the the base with indium and fixed by a tantalum cup. The puck is mounted on the cathode holder during evaporation and photo-electron emission.	35
4.7	The picture of the evaporation sources. The evaporation sources are mounted on a linear stage in the chamber. K and Cs can be set each of three in the evaporation sources. The Sb pellets were resistively heated in a tungsten evaporation basket.	35
4.8	A vertical view of the arrangement around the cathode puck. The thickness monitor and the cathode puck were placed in symmetrical positions to the evaporation source. The cathode puck temperature is controlled by a heater from the backside.	36
4.9	Etching procedure of Si substrate. The Si(100) and Si(111) substrates were processed with a 5% HF solution for about 5 min.[106]	37
4.10	Etching procedure of GaAs substrate. The GaAs surface was processed with a $\text{H}_2\text{SO}_4:\text{H}_2\text{O}_2:\text{H}_2\text{O}$ (4:1:1) solution for about 1 min[90] and to make As rich surface.	37
4.11	Heat cleaning. The substrate is heated up to 600°C in vacuum. Temperature is shown red line and vacuum pressure is shown blue line during the heat cleaning.	38
4.12	QE evolution and progress of thickness of Sb, K, and Cs. QE evolution is shown red circle and progress of thicknesses of Sb, K, and Cs are shown blue triangle. QE appears in K evaporation and increases rapidly in Cs evaporation. The thickness are 10nm, 70nm and 1400nm for Sb, K and Cs, respectively.	39
4.13	The maximum QE is shown as a function of temeperature during the evaporation with blue squares and red circles for the Si(100) and Si(111) substrates, respectively. The error on the horizontal axis is fluctuation during evaporation and the error on the vertical axis is statistical error by 3 times measurements.	40

4.14	The maximum QE is shown as a function of Sb thickness with blue squares and red circles for the Si(100) and Si(111) substrates, respectively. The error on the horizontal axis and error on the vertical axis are only statistic.	41
4.15	The comparison of QE evolution during the cathode evaporation for the cleaned substrates are shown with red circles, blue triangles, and green squares for the cleaned Si(100), Si(111), and GaAs(100) substrates, respectively. QE appears in K evaporation and increases rapidly in Cs evaporation. K evaporation started on 48, 45 and 45 min for the cleaned Si(100), Si(111), and GaAs(100) substrates, respectively. Cs evaporation started on 183, 175 and 135 min for the cleaned Si(100), Si(111), and GaAs(100) substrates, respectively.	42
4.16	The comparison of QE evolution during the cathode evaporation is shown with red circles, blue circles, and green circles for the as-received Si(100), Si(111), and GaAs(100) substrates, respectively. In the blue, green, and yellow shaded regions, Sb, K, and Cs were evaporated, respectively. The QE appears in the K evaporation and increases rapidly in the Cs evaporation.	43
4.17	Atomic arrangement of CsK ₂ Sb(100) on the Mo(100), GaAs(100) and Si(100) surfaces. The lattice constants of Mo, Si, and GaAs are 3.15Å, 5.43Å, and 5.65Å, respectively [111].	45
4.18	Atomic arrangement of CsK ₂ Sb(111) on the Si(111) surface.	46
5.1	A schematically drawing of the sample gas introduction system. The system and the main chamber are connected by a leak valve to control the gas introduction rate. The gas species can be changed by toggling valves to each gas bombs. The system is evacuated by a rough pump for every gas switching to avoid gas mixture.	48
5.2	QE evolution during the activation process by Cs and O ₂ . The first peak is made by Cs only. In other peaks, QE is increased by O ₂ and decreased by Cs.	49
5.3	QE evolution of the activation process with Cs and CO ₂ . The activation procedure was same as that with O ₂ except the introduced gas.	50
5.4	QE evolution during the activation process with Cs and CO. QE did not rise with CO. After t=0.9 h, the NEA activation was performed by Cs and O ₂ . The solid line is that with CO gas introduction and the dashed line is that by O ₂	51

5.5	QE evolution of the activation process with Cs and N ₂ . After t=1.05 h, the NEA activation was performed with Cs and O ₂ . The solid line is that with N ₂ gas introduction and the dashed line is that with O ₂	52
5.6	The height of each peak in Fig.5.2 is shown as a function of O ₂ gas exposure. The red solid line is a fitting curve by assuming Eq. (5.4).	53
5.7	The height of each peak in Fig.5.3 is shown as a function of CO ₂ gas exposure. The red solid line is a fitting curve by assuming Eq. (5.3).	55
A.1	The band structure of GaAs and the state of excitation by photons to the conduction band. (a) shows bulk GaAs crystal, (b) is a diagram of distorted GaAs crystal. Degeneracy of angular momentum 3/2 state is solved by distortion.[20]	67
B.1	Atomic arrangement of CsK ₂ Sb(100) and CsK ₂ Sb(111) on the Mo(100), GaAs(100), Si(100), and Si(111) surfaces. The lattice constants of Mo, Si, and GaAs are 3.15Å, 5.43Å, and 5.65Å, respectively [111]. .	68
B.2	ζ is obtained with the atomic positions of the substrate and CsK ₂ Sb by Eq. B.1. By rotating angle θ , we take the minimum value as a representative matching index.	69
B.3	$\zeta(100)$ is calculated as a function of the rotation angle θ for CsK ₂ Sb(100) and the various substrates.	71
B.4	$\zeta(110)$ is calculated as a function of the rotation angle θ for CsK ₂ Sb(110) and the various substrates.	72
B.5	$\zeta(111)$ is calculated as a function of the rotation angle θ for CsK ₂ Sb(111) and the various substrates.	73

Abstract

The accelerator has contributed greatly to develop many scientific discipline, e.g. elementary particle/nuclear physics, synchrotron radiation sciences including material physics, bio-science, industrial applications, medical applications, etc. Although the electron storage ring has been widely used as the advanced accelerator for the electron and positron collider and the third generation light source, the beam performance of these ring accelerators is strongly limited by two aspects by the synchrotron radiation. One is the large energy loss limiting the beam energy practically up to 120 GeV. Another is the equilibrium state limiting the beam emittance, especially in horizontal direction. To obtain the better beam performance breaking the limits by the ring, Linac (Linear Accelerator) is revived. The electron source is one of the most important device in Linac, because the performance of the accelerated beam strongly depends on the initial beam quality. A photo-cathode is able to generate a high-performance electron beam with a large operability. The thesis addresses a couple of studies for the advanced photo-cathode. The first is a study of CsK₂Sb cathode. This cathode is driven by a green light laser (532 nm) with high quantum efficiency(QE) 10%. It is fabricated as a thin film by vacuum evaporation on a substrate. We found that the performance strongly depends not only on the substrate material and its chemical state (oxidized, etc.), but also on the surface direction of crystal substrate. This is the first experimental evidence in the world. The second is the NEA (Negative Electron Affinity) activation of GaAs photo-cathode with N₂, CO, and CO₂ gases. NEA-GaAs cathode is able to generate highly spin polarized electron beam more than 90% and the NEA activation is performed usually with Cs and O₂ or NF₃. We found that CO₂ activated the cathode, but N₂ and CO did not. By analyzing CO₂ activation, CO degrades the NEA activated surface, and the NEA activation ability of atomic O is almost a half of that of O₂ molecule. The NEA activation with CO₂ and measuring the activation ability of CO₂, O₂, and atomic O are the first experimental efforts.

Acknowledgments

First, I would like to thank my supervisor, Dr. Masao Kuriki, for his continuous support.

I would also like to thank Dr. Hiromi Okamoto, Dr. Hiroyuki Higaki and Dr. Kiyokazu Ito for his technical guidance on experiments throughout my research.

I want to thank the other members of the Beam Physics Laboratory at Hiroshima University.

Finally, I thank my wife for supporting me.

And this work is partly supported by Photon and Quantum Basic Research Coordinated Development Program from the the Ministry of Education, Culture, Sports, Science, and Technology, Japan and Cooperative supporting Program for Research and education in University by KEK(High Energy Accelerator Research Organization), Japan.

Chapter 1

Introduction

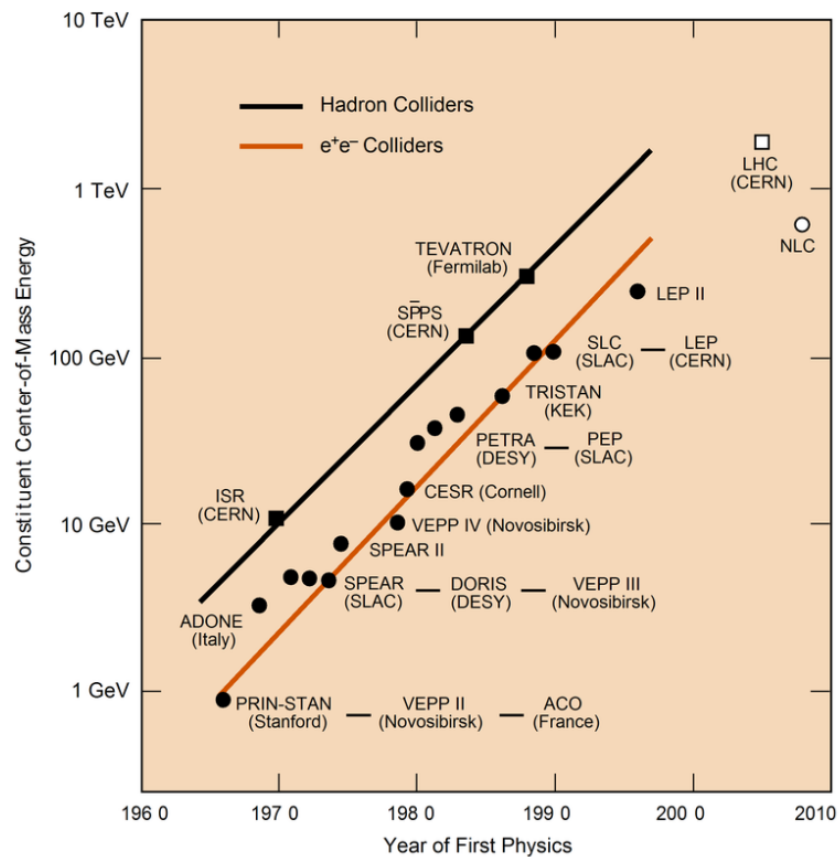


Figure 1.1: Livingston plot, in which the horizontal axis represents year and the vertical axis represents acceleration energy, indicating that the energy increased rapidly in time.[1]

Accelerator is a device that boosts the particle energy as its name suggests. It is no exaggeration to say that the first half of the particle accelerator history

is the history of elementary particle and nuclear physics. Figure 1.1 is Livingston plot[1], in which the horizontal axis represents year and the vertical axis represents acceleration energy, indicating that the energy increased rapidly in time. Particle physics has been developed as the accelerator energy has been increased. Electron and positron colliders with storage rings have been a powerful tool to explore the particle physics since 1960s. The examples are VEPP[2], SPEAR[3], DORIS[4], TRISTAN[5], LEP[6], CESR[7], BEPC[8], PEP[9], KEKB[10], etc. In the 1960s, many "elementary particles" were discovered by accelerators. Later, they were understood as composite particles of quarks and gluons. The deep inelastic scattering of high energy electrons with nucleon revealed the structure of the nucleus and that was an experimental evidence of the quark model. In the 1970s, the discovery of J/Ψ particles, which is the binding state of c quarks, and in the 1980s, W Boson and Z Boson which are gauge particles that mediate weak interaction were discovered. In 1990s, LEP (Large Electron Positron collider)[6] which is an $e^+ e^-$ ring collider, and SLC (SLAC Large Collider)[11] which was the first $e^+ e^-$ linear collider, studied the detail of Z Boson property. In 2012, the Higgs Boson which was the last piece of the standard model was discovered by LHC (Large Hadron Collider) at CERN. Since electron and positron are elementary particles having no structure and are anti-particle to each other, it is possible to study any energy state reachable by CME (Center of Mass Energy) with the well-defined initial state. The $e^+ e^-$ colliders greatly contribute to establish the standard model of particle physics.

After top quark was discovered by TEVATRON at Fermi national laboratory, USA, Higgs particle was "the last piece" of the standard model. It is theoretically predicted, but it was not discovered yet. Although LEP had tried to find Higgs particle by scanning its energy up to 209 GeV CME, it could not. Finally, Higgs particle was discovered by LHC which is a proton-proton collider with 8 TeV CME. The proton collider is reachable such high energy region, but the initial state is not fixed because the proton is a composite particle. To study the detail property of not only Higgs, but also top quark and any new particles, we need e^+ and e^- collider in several 100 GeV CME or higher. CME energy of Higgs production through ZH process is peaked at 250 GeV. Top pair production is on 350 GeV CME. On the other hand, it is not realistic to increase the energy of the e^+ and e^- ring collider further to this energy region, because the synchrotron energy loss is proportional to the fourth order of the beam energy. The energy loss of LEP at 209 GeV CME was 2 GeV per turn. If we consider 500 GeV CME, the energy loss becomes 66 GeV per turn. Obviously, it is not manageable by considering the huge space for accelerator in the ring or the huge electricity.

Instead of the ring e+ e- collider, e+ e- linear collider has been considered since 1980s as the next generation e+ e- collider. In linear collider, the beam is accelerated by linear accelerator. The beam orbit is in line and the synchrotron radiation is negligible. High energy physics society and ICFA (International Committee for Future Accelerator) announced to promote International Linear Collider (ILC) project[12] as the next high energy physics project in 2004. ILC is an electron-positron collider with superconducting linear accelerators. In linear collider, determination of the initial state as precise as possible is essential to maximize the physics ability. That leads that the spin state of electron and positron should be aligned to one direction, polarized. A highly spin polarized beam is strongly demanded by linear colliders.

Another big usage of accelerator than the particle physics is the synchrotron radiation science. synchrotron radiation was theoretically predicted in 1946. SR is emitted when a charged particle receive any force. It has been experimentally confirmed in an electron synchrotron in the following 1947. The synchrotron radiation power is proportional to the fourth power of the beam energy and rapidly increases as energy increases. The synchrotron radiation is merely an energy loss from the viewpoint of increasing the energy of particles as we mentioned, but it is applicable as a light source, because it has high brightness, high directive, polarization, pulse characteristics, etc. The use of synchrotron radiation began as a parasite. It was called as the first generation light source. The second generation light source is a dedicated accelerator (electron storage ring) as the synchrotron radiation source. The examples are NSLS[13], BESSY[14], Photon Factory[15]. The third generation light source is a storage ring incorporating a magnet (wiggler or undulator) dedicated and optimized to generate the synchrotron radiation and the storage ring was optimized for low emittance. The third generation light source is a completed scheme of the Synchrotron Radiation source based on an electron storage ring. The examples are ESRF[16] and NSLS II[17], Spring-8[18], and MAX IV[19].

Although demands for the synchrotron radiation light is improved in time, such as short pulse, high coherence, becomes higher and higher, the storage ring based light source has limitations on the performance in principle. The pulse length and emittance of the beam are determined as an equilibrium state of quantum excitation and radiation damping in a storage ring. The pulse length(σ) of the beam stored in a storage ring is determined as[20],

$$\sigma = \frac{\sqrt{2\pi}c}{\omega_{rev}} \sqrt{\frac{\eta_c E_0}{heV \cos \phi_s} \frac{\sigma_E}{E}} \quad (1.1)$$

where ω_s is the revolution frequency, σ_E is energy spread, η_c is momentum com-

paction factor which is the ratio of the variation of the revolution period to the momentum, V is the RF voltage, E is the beam energy. To obtain a short pulse, the RF voltage for re-acceleration should be large, but it has technical limitation. The practical limit on the bunch length is in order of 10s ps. The ultra-short pulse such as ps or sub-ps cannot be generated with the third generation light source.

Coherence is a typical property of waves. High coherence light is useful in various contexts. For example, by using phase information of light, structure analysis for a huge molecule such as protein is possible without crystallization. To make high coherent light as the synchrotron radiation, the electron bunch size should be “point like” comparing to the wavelength of the light. That means short pulse and low emittance. We have already mentioned that the storage ring has limitation on the bunch length. The emittance in the storage ring is expressed as[20]

$$\epsilon_x = \frac{C_q \gamma^2}{J_h} \frac{1}{2\pi\rho^2} \int H ds \quad (1.2)$$

where C_q is a constant, J_h is damping partition number, γ is Lorentz factor, ρ is the radius of curvature of the bending electromagnet, $\int H ds$ is a function of momentum dispersion. To minimize the emittance, the momentum dispersion should be small, but there is a limitation in principle. There is a practical limitation on the orbit radius, too. The practical limit on the emittance of the storage ring can be in order of 0.1 nm·rad. In short, it is difficult to obtain the coherent hard X-ray with the third generation light source.

Linac based synchrotron radiation facility can realize such short pulse and high coherent light. The linear accelerator is that accelerates the charged particle with periodic RF structures aligned in line. The beam geometry in the linear accelerator is independently determined from the lattice structure. Then, if one can generate the low emittance beam and can accelerate the beam without a significant emittance growth, an extremely low emittance beam can be obtained. That is also true for a short pulse beam. In Linac, higher electricity consumption per beam current is an issue, because the beam is not re-used (circulated). Energy Recovery Linac (ERL)[21][22] is a solution to cure the problem. In ERL, the beam energy is transferred from the used beam to the new beam. The beam is always fresh, but most of the beam energy is re-used. ERL generates a high intensity beam with a small emittance and short pulse length in CW. ERL can be an ideal facility for users which requests an extremely small emittance and short pulse such as Laser-Compton X-ray source.

A highly coherent synchrotron light can be obtained with FEL (Free Electron Laser)[23] based on Linac. FEL consists from a Linac and undulator which is a

device making the transverse magnetic field changing the sign periodically. If a low emittance beam with a large peak current passes through the undulator, a dense synchrotron radiation light will be emitted. If the light has a small coherence, the electro-magnetic field by the light modulates the electron bunch intensity which increases the coherence. The improved coherence on the beam enhances the coherence and power of the synchrotron light. This positive feedback process between the bunch intensity modulation and coherent synchrotron radiation results a high intensity coherent synchrotron radiation. This is called as FEL.

As we explained, Linac is expected to be a break-through in the particle physics and synchrotron radiation science. In Linac, the beam emittance is determined by the initial beam emittance from the electron source and emittance growth effect such as space charge effect, coherent synchrotron radiation in bending magnet, etc. To minimize the beam emittance of a linear accelerator, the initial emittance should be small enough with good emittance growth compensation. The beam source is one of the most important subsystem in linear accelerator.

There are four physical process to generate electron beam; thermionic emission, photo-electro emission, field emission, and secondary emission. Among them, thermal emission and photo-electro emission are popular as the electron source for accelerator. By employing a short pulse laser, photo-electro emission can generate a short pulse electron beam directly with a large operability. The electron source by the photo-electro emission with the short pulse laser is considered to be the advanced technology for the electron beam generation[24]. The material to generate the photo-electron is called as photo-cathode.

Among various photo-cathode materials, CsK₂Sb and NEA GaAs cathodes are the most advanced one.

CsK₂Sb is a semi-conductor fabricated as a thin film by vacuum evaporation technique. The material can be driven by visible green light (532 nm) for the photo-emission with more than 10% QE[25][26]. The material is robust against to a large emission current[27]. Due to these characters, CsK₂Sb is one of the best candidate for high brightness electron source (a large current density). This is the baseline design of LCLS II project[28], which is the first CW X-ray FEL project in US. A large current up to 0.3 mA is required with 0.4 mm·mrad emittance.

It is well known that the cathode performance depends on the substrate material and surface condition[25] [29] [30] [31]. In this thesis, we studied the cathode performance dependence systematically on the substrate material, surface state, and surface direction to improve the performance and its reproducibility.

NEA GaAs photo cathode is a unique device which is able to generate highly spin polarized electron beam up to 90% and an extremely small emittance beam.

The photo-electron emission is possible with IR (Infrared Red) and visible light and the QE can be more than 20%. This is the only solution of highly spin polarized electron source for accelerator[32][33]. The spin polarized electron beam has a crucial role in ILC project[12].

The NEA surface is a surface state in which the energy level of the vacuum is lower than the lowest level of the conduction band. The surface is artificially made by an activation process with Cs and Oxygen or NF_3 evaporation on a cleaned P-type GaAs. The NEA surface is fragile and easily damaged by residual gas adsorption or beam extraction. At present, there are some hypotheses, but the structure of the NEA surface is not understood well. To improve our understanding for the NEA surface, we performed the NEA activation process with other gases than O_2 .

In Chapter 2, we explain the advanced accelerator projects based on Linac from the technical point of view of electron beam generation.

In Chapter 3, the general aspects of photo cathode are explained.

In Chapter 4, the experiment and analysis for the substrate dependence of CsK_2Sb are explained.

In Chapter 5, the experiment and analysis for the NEA GaAs activation with other gas than O_2 are explained.

In Chapter 6, we summarize our studies and discuss possible impacts on the accelerator science.

Chapter 2

Photo cathode in modern accelerators

As we explained in the previous chapter, there are a bunch of the next generation accelerator projects based on Linac. Because Linac has an open topology and this is a simple response system, a good beam as the input is required in order to obtain a good beam as the output. Because the beam performance of the input is determined by the cathode and the gun configuration, the gun is much more important in Linac than that in the ring accelerator. In this Chapter, the cathode in the advanced accelerators is reviewed.

2.1 ERL

ERL is a new accelerator concept initially proposed by M. Tigner for linear collider[34]. The advantage of Linac is the beam quality, but the dis-advantage is large electricity consumption per beam current. The required wall plug power by Linac P_{Linac} is

$$P_{Linac} = \frac{IE}{\eta}, \quad (2.1)$$

where I is the average beam current, E is the beam energy in eV, and η is the power efficiency converting from the wall plug power to the beam power. The efficiency depends on the technology and the maturity, but it is in order of 10%. The wall plug power is several times of the beam power. On the other hand, the wall plug power in a ring accelerator, P_{ring} is

$$P_{ring} = \frac{IE}{\eta\tau}, \quad (2.2)$$

where τ is the lifetime of the stored beam. The stored beam in a ring is lost by several effects such as beam scattering with residual gas and the beam current is

exponentially decayed. For the ring, the electricity is determined by not the beam current (stored current), but the lost current, leading the much better efficiency of the electricity per the beam current. Please note that the synchrotron radiation loss is ignored here. If the beam energy is large, so that the synchrotron radiation energy loss becomes significant, the advantage of the ring is lost.

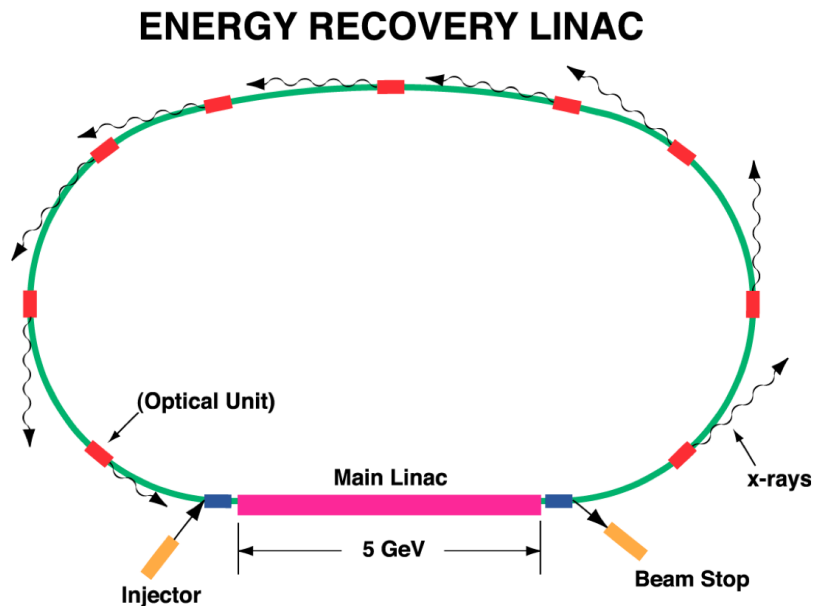


Figure 2.1: An overview graphic of the ERL.[35].

To compensate the electricity of Linac, ERL concept is considered. The electron beam is accelerated and the accelerated beam is injected to the accelerator again through a return path, but it is on the decelerated phase. The beam is decelerated along the accelerator and the energy is transferred from the beam to RF power in the cavity. In ERL, the beam is continuous, i.e. the accelerated beam and the decelerated beam exist in the accelerator simultaneously. The power extracted from the decelerated beam is moved to the accelerated beam. The electricity is much suppressed as

$$P_{ERL} = \frac{I\chi E}{\eta}, \quad (2.3)$$

where χ is the fraction of the injection energy to the full beam energy, because the injection energy is not recovered. The topology of ERL is same as Linac if we follow the electron beam trajectory, but the topology is torus (ring) if we follow the power flow. Here we ignore the power dissipated in RF accelerator. To maximize the merit of ERL, a super-conducting RF accelerator is the choice.

Because the beam is always fresh, ERL can generate a short pulse and coherent light. ERL performance surpasses that of third generation light source with an

Table 2.1: Electron beam parameter of ERL project [21][22][37]

	3GeV ERL radiation source	cERL
Orbiting energy	3 GeV	60-85 MeV
Average current	10-100 mA	10-100 mA
Normalized emittance	0.06-1 π mm·mrad	0.1-1 π mm·mrad
Electronic bunch length	0.1-3 ps	0.1-3 ps
Electron bunch charge amount	7.7-77 pC	7.7-77 pC
Repetition frequency	1.3 GHz	1.3 GHz

equivalent power consumption. For example, an X-ray light source using ERL can generate X-rays having spatial coherence and ultra-short pulse X-rays in femtosecond which opens up new X-ray sciences. Gamma ray source by the laser-Compton scattering based on ERL realizes a large flux that exceeds the existing gamma ray source by 6 to 8 orders of magnitude, and has a great impact on the research such as photo-nuclear science and industrial application such as non-destructive isotope analysis[21][22][36].

Figure 2.1 shows an example of ERL designed for synchrotron radiation facility which is capable to generate X-ray in the diffraction limit. It consists from a 5-15 MeV injector, a 400 m long super-conducting linac, two 800 m return arcs, and a beam dump line. The beam is dumped after it is decelerated down to the injection energy. The injection beam energy is equal to that in beam dump in principle, which limits the power efficiency.

The electricity is much compensated by employing ERL, but the injector has to provide a large current which is equivalent to the beam current. Because providing a high performance beam which is superior to that of a storage ring is the aim of ERL, the electron source of ERL has to provide a large current, short pulse, and small emittance beam.

Currently, the development of the next-generation synchrotron source by ERL is under way in Japan and US[21][37]. In Japan, KEK, QST(National Institute for Quantum and Radiological Science and Technology), University of Tokyo, Nagoya University, and Hiroshima University are jointly developing a test machine[37].

Tables 2.1 and 2.2 show parameters of an example of ERL facility and the electron gun, respectively. The electron bunch length is 0.1-3 ps which is 10-100 times shorter than that of Spring-8[38]. Emittance is several or several ten times lower than that of Spring-8 whose horizontal normalized emittance is 48 π mm·mrad, with an equivalent beam current.

Table 2.2: Parameters of electron gun for ERL[21][22]

	Electron gun for ERL
Energy	500 kV
Average current	10-100 mA
Normalized emittance	0.1-1 π mm·mrad
Electronic bunch length	0.1-3 ps
Electron bunch charge amount	7.7-77 pC
Repetition frequency	1.3 GHz

The ERL gun has to provide 100 mA beam current with a high quality continuously. This is 10^4 times more than that for a conventional electron source for accelerator. That leads several issues on the electron source which will be discussed in detail later.

2.2 FEL

As briefly explained in 1, FEL is a kind of laser whose lasing medium is electrons moving freely through undulator field[39][40]. FEL can achieve very high peak power, tunability (covering from microwave to X-ray), coherence which are desirable in many disciplines of synchrotron sciences. The conceptual diagram of FEL is shown in Figure 2.2.

In FEL, a small intensity modulation along the electron bunch in a wavelength is amplified through FEL process. The initial modulation is noise in Self-Amplified Spontaneous Emission (SASE) mode, but it is artificially generated in pre-bunched FEL mode. The intensity modulation leads a high power radiation with a coherence and the high power radiation enhances the intensity modulation. This results exponential growth of the power of the coherent radiation. High power radiation is obtained finally[41].

Table 2.3 shows the parameters of the Linac Coherent Light Source (LCLS) which is an X-ray FEL in operation at SLAC. Comparing to the 3rd generation light source, the average current of LCLS is quite low, but the peak current is high which is essential for FEL. LCLS employs a metal photo cathode, Cu. It requires a high power UV light for electron generation, but an ordinal laser technology is able to deliver such laser pulse, because the reputation is low.

LCLS, Euro XFEL(DESY), and SACLA(Spring-8) are pulse XFEL, i.e. X-ray laser is provided in pulse. To improve the X-ray laser power, CW operation is the next step. LCLS II in SLAC[28] which is a CW X-ray FEL, is under

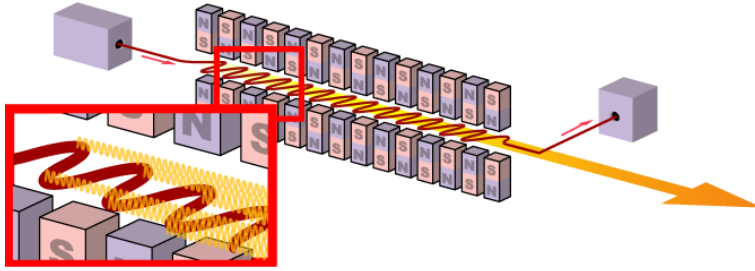


Figure 2.2: The conceptual diagram of FEL.[42]

Table 2.3: Parameters of the electron beam for LCLS[43]

	LCLS
Electron energy	4-14 GeV
Bunch charge	0.1-1.0 nC
Bunch repetition rate	120 Hz
Peak current	3.4 kA
Average current	$< 1 \mu\text{A}$
Normalized emittance	$1.2 \pi \mu\text{m}\cdot\text{rad}$
Bunch length	230 fs

construction. LCLS-II is constructed from the success of LCLS. It delivers photons between 200 eV and 5 keV at repetition rates as high as 1 MHz (929 kHz) using a superconducting RF (SCRF) Linac.[28].

LCLS II employ 186 MHz (the 7th sub-harmonics of 1.3GHz) RF Gun which is originally developed by LBNL (Lawrence Berkeley National Laboratory), USA. The gun has to provide high current and low emittance beam continuously. Table 2.4 shows the parameters of the LCLS-II. The metal cathode is robust, but it is not feasible for the high current generation, because an extremely high power UV laser is required to generate the beam, since the QE is in order of $1e-4$. Cs_2Te semi-conductor cathode can be a candidate, because 1% QE can be maintained for a long period, but it is not ideal, because it requires still UV light for photo-emission. CsK_2Sb is the best candidate for the cathode because it is driven by a green laser. The green light can be generated as SH(Second Harmonic) of a solid laser a much better efficiency than that of UV laser. The 10% high QE is also a big advantage. CsK_2Sb is feasible for the continuous high current operation since it is robust enough to generate in order of 10mA beam current. In Chapter 3, we discuss the status and issues of the cathode.

Table 2.4: Parameters of the electron beam for LCLS II.[44]

	LCLS II
Electron energy at gun exit	750 keV
Electron energy	4 GeV
Bunch charge	100 pC
Bunch repetition rate	1 MHz
Peak current	10 A
Average current	0.062 mA
Normalized emittance	$0.4 \pi \mu\text{m}\cdot\text{rad}$
Average CW RF gradient	16 MV/m

2.3 Linear Colliders

To study the detail property of not only Higgs, but also top quarks and any new particles, we need e+ and e- collider of 250 GeV or higher CME. It is not realistic to increase the energy of the e+ and e-ring collider further, because the synchrotron energy loss is proportional to the fourth order of the beam energy. Instead, e+ e- linear collider has been considered since 1980's as the next generation e+ e- collider. In linear collider, determination of the initial state as precise as possible is essential to maximize the physics ability. That leads that the spin state of electron and positron should be aligned to one direction, polarized. A highly spin polarized beam is strongly demanded by linear colliders.

ILC is a 250-500 GeV CME (extendable to 1TeV) electron-positron collider, based on 1.3 GHz superconducting radio-frequency (SCRF) linear accelerator as shown in Figure 2.3. Kitakami mountain area, Iwate prefecture of northern Japan, is the candidate site of ILC[45]. ILC is 30 km long for 500 GeV CME and 50 km for 1 TeV CME [46]. ILC can be characterized as

- A polarised electron source based on a photocathode DC gun.
- A polarised positron source obtained from pair creation by circularly polarized gamma ray generated by helical undulator.
- 3.2 km 5 GeV electron and positron damping rings (DR) for the extremely low emittance beam in vertical direction.
- Two 11 km main linacs with 1.3 GHz SCRF accelerator operating in 31.5 MV/m.

- Final focus system which focuses the beam size down to 7 nm in vertical direction for the high luminosity.

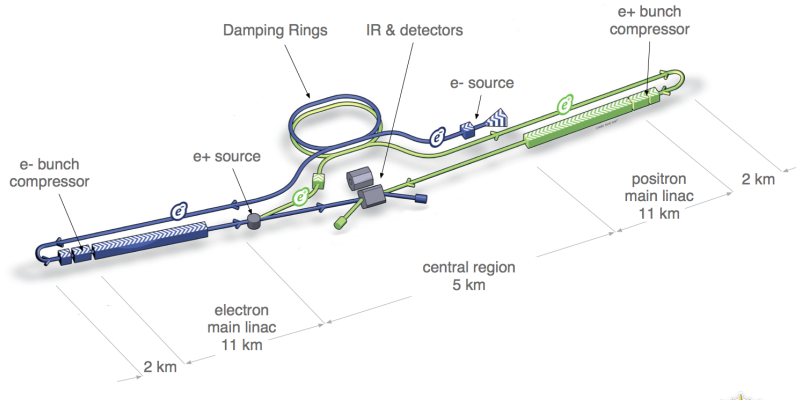


Figure 2.3: A schematic overview of ILC layout based on the accelerator design described in Technical Design Report.[47]

Compared to LHC[48] which is a high energy proton-proton collider, the CME (Center of Mass Energy) of LHC and ILC are up to 14 TeV and 1 TeV, respectively. Because LHC is a proton-proton collider, only a part of the CME contributes to the reaction and there are many background events. CME of each event is statistically distributed for proton collider and the initial state is basically not decidable. On the other hand, ILC CME is lower, but CME is fully used for reaction and there are few background events. The initial state of the interaction is well defined. Therefore, ILC can search any phenomena in a clean experimental environment with a high accuracy, even if the final state is invisible.

The electron beam parameters at the gun exit of ILC are shown in Table 2.5. Since the extremely low emittance beam is formed by DR (Damping Ring), emittance of the electron beam from the electron gun doesn't have to be small. The most important parameter is the bunch charge (3.2 nC) and polarization (more than 80%). This large bunch charge is essential to obtain a large luminosity together with the extremely small emittance at the interaction point. The polarization is essential to define the initial state and decrease the background event such as W-W scattering to perform the accurate measurement[49]. The spin polarization is defined as

$$P = \frac{N_+ - N_-}{N_+ + N_-} \quad (2.4)$$

NEA-GaAs cathode is the only option to meet the ILC requirements, i.e. more than 80% spin polarization. In ILC[12], the GaAs/GaAsP strained super-lattice

Table 2.5: The electron beam parameters at the gun exit of ILC.[50]

Electron gun for ILC	
Polarization degree	>80%
Bunch charge	3.2 nC
Normalized emittance	10 $\mu\text{m}\cdot\text{rad}$
Electronic bunch length	1 ns
Bunch interval	308 ns
Macro pulse length	0.9 ms
Average current	5.2 mA (in pulse)

crystal is employed. The NEA surface is essential to generate the highly spin polarized electron. Because the NEA surface is sensitive to residual gas pollution and ion-back bombardment, this cathode is not compatible to RF gun and is used only in a DC electron gun. The structure of NEA surface is not understood well. Understanding the NEA surface and improving the cathode robustness are important not only from the fundamental physics point view, but also the practical view point. NEA GaAs cathode is also useful as a high brightness (large current and small emittance) electron beam, due to the small beam emittance[51]. In Chapter 3, we explain the NEA-GaAs cathode in detail.

Chapter 3

Photocathode

As explained in the previous chapter, several advanced accelerators based on Linac has been constructed and proposed to break the limitations of the ring accelerator. The photo-cathode has a crucial role in these accelerators. The initial beam property is more important in Linac than that in ring, because the accelerator performance depends on the initial beam. CsK₂Sb and NEA-GaAs cathode are the key components of CW FEL/ERL and ILC, respectively. In this chapter, we discuss general aspects of photo cathode materials and property of CsK₂Sb and NEA GaAs regarding to the beam performance in detail.

3.1 Metal cathode

The most popular photo-cathode material is a metal such as Cu[52], Mg[53], or Ag[54]. Metal photocathode is used in a high gradient RF guns due to the high robustness, such as S-band BNL gun IV[55]. LCLS employs the S-band RF Gun with Cu photo-cathode to provide a high bunch charge and low-emittance beam for X-ray FEL. The LCLS gun is operated for over a year without exchange the cathode[56]. The metal cathode is robust, so that it can be transferred in air without any significant performance degradation. Due to the large work function of the metal which is typically more than 3 eV, ultra-violet (UV) light is required for photo-electron emission. The QE of photo-electron emission is typically in order of 0.01% or less. Therefore, it requires a high power UV laser to generate a high current beam. It is difficult to generate UV light directly and harmonic generation technique is employed[57]. The UV light is obtained as the third or fourth harmonics of the fundamental laser light such as Ti:Sapphire or Nd:YAG lasers. The harmonic generation is performed with a birefringence crystal. The conversion efficiency is usually much less than unity, and the laser system becomes

complex. The harmonic generation is a non-linear phenomena enhancing the power fluctuation in principle, and it degrades stability.

Metal has a limited penetration depth of photon to inside the material. That is a reason of the low QE, but it leads the extremely fast response to the photo-emission. It is as fast as cannot be measured accurately.

The beam emittance from a metal cathode is [20],

$$\varepsilon = \frac{R}{2} \sqrt{\frac{\hbar\omega - \phi}{3mc^2}} \quad (3.1)$$

where R is the beam size, \hbar is Planck constant, ω is angular frequency of laser, ϕ_0 is work function of the material, mc^2 is electronic static mass. The emittance can be minimized by adjusting the laser frequency to the work function. Please note that the thermal contribution to the emittance is ignored in Eq. 3.1. If the laser contribution is negligible, the thermal contribution becomes significant, but the contribution is usually small.

QE as a function of the laser frequency is expressed as

$$\eta(\hbar\omega) \sim \eta_0(\hbar\omega - \phi_0)^2, \quad (3.2)$$

which means the QE is approaching to zero by the adjustment. The high QE and the low emittance are not compatible in metal cathode.

According to the property, metal cathode is feasible to generate a short pulse electron beam, but low repetition rate. A good emittance beam can be generated, but it requires a more laser power. Metal cathode is not feasible as cathode for ERL or CW FEL due to the low QE. LCLS uses Cu cathode, but LCLS II which is CW FEL, will employ CsK₂Sb.

3.2 CsK₂Sb photocathode

CsK₂Sb is called as multi-alkali cathode because it composed from more than one alkali metal. CsK₂Sb is a direct transition type semi-conductor with 1.2 eV band-gap energy [58]. It is formed as thin film layer with vacuum evaporation technique[59]. It has been used as photo-cathodes in photo-multiplier tubes[60] and in a few electron guns[61][62].

CsK₂Sb forms a DO₃ cubic structure[63]. The unit cell contains four formula units and is represented by four face-centered sub-lattices shifted by $a\sqrt{3}/4$ (a is a lattice constant of the primitive translation vector) along the body diagonal [63][64]. The lattice constant a is 8.61 Å[63][65][66].

CsK₂Sb cathode is fabricated as a thin film on a substrate by evaporation in an ultra-high vacuum environment. Typically the CsK₂Sb cathode was formed by sequential evaporation of Sb, K, and Cs on a substrate[67].

The CsK₂Sb cathode showed relatively high QE as 7-10% with 532nm laser light[25][26][68]. The cathode is robust enough for a high current beam generation as demonstrated by Cornell University (60 mA about 30 hours)[69]. The CsK₂Sb photocathode can reliably exhibit high QE like NEA-GaAs, and has a slightly larger thermal emittance as compared to the NEA-GaAs[70], which would affect the maximum brightness of its electron beam, but it is considered to be a prompt emitter because of its PEA(Positive Electron Affinity) nature, producing shorter electron bunches than GaAs. CsK₂Sb cathode is the most promising candidate for high brightness electron source due to high QE, green excitation and long life.

Since CsK₂Sb cathode has PEA, it is difficult to extract the polarized electrons as same as metal cathode.

Because CsK₂Sb cathode is generated by vacuum evaporation and is oxidized immediately in air due to the high chemical activity of alkali metal, the material property is not well understood. For example, many materials have been used as the substrate of the evaporation, glass[71], Cu(amorphous)[72][29], SUS[29][30][31], Mo(amorphous)[29][31], Mo(100)[25], Si(100)[26], GaAs(100)[68], where the numbers in parenthesis are the surface direction of the crystalline substrate.

Cs₃Sb cathode has proven to depend strongly on the chemistry of substrate surface[59]. XPS studies for the CsK₂Sb cathode[31][73] suggest that the cathode performance strongly depends on the substrate surface state (oxidation, etc.).

Cathodes fabricated on the amorphous substrates (glass, Cu, SUS, and Mo) showed relatively low QE as 1-5% with 532nm laser light[71][72][29][30][31]. In contrast, cathodes fabricated on crystalline substrates (Si(100), Mo(100) and GaAs(100)) showed relatively high QE as 7-10% with 532nm laser light[25][26][68]. These results suggest that the substrate crystallinity has an impact on the cathode performance.

CsK₂Sb crystal direction was studied with XRD[74][75]. In the first study[74], the crystal was grown in (200) direction on Si(100) at room temperature(RT) and grown in (220) direction at 100 °C. On the other hand, in the second study[75], the crystal was grown in (200) direction on Si(100) at RT and 100 °C. The QE of the cathode in these studies was relatively low (3 %) and the cathode performance dependence on the surface direction of the substrate or CsK₂Sb crystal was not significantly observed. One possibility is that the cathode evaporation condition was not fully optimized in these studies.

Although the cathode performance depends on the substrate material as de-

scribed, any universal reason is not established yet. To establish the universal understanding for the dependence is one of the purposes of this thesis.

In Chapter 4, we performed cathode evaporation on Si(100), Si(111), and GaAs(100) substrates to evaluate the performance dependence on the substrate material and surface state systematically.

3.3 NEA-GaAs photocathode

GaAs is a III-V semiconductor having a direct band gap of 1.4 eV at room temperature. Fermi level is in the middle of the forbidden band, and the work function is 4.3 eV. The first formation of NEA on the GaAs surface was reported adsorbing Cs on p type GaAs(110) by Scheer and Laar in 1965[76]. Since then, researches on GaAs cathode have actively been made.

The NEA surface is a surface state in which the energy level of the vacuum is lower than the lowest level of the conduction band. The NEA surface on GaAs is artificially generated by a so-called "Yo-Yo method" in which Cs and Oxygen/NF₃ are applied on a clean p-type GaAs semiconductor surface. At present, there are some hypotheses, but the structure of the NEA surface is not determined. One example is the electric dipole hypothesis; Cs and oxygen form an electric dipole layer on the surface [77].

Figure 3.1 shows the electronic level of the NEA GaAs cathode and the photoelectron emission. Electrons excited to the conduction band by the laser photon. The electron diffuses thermally through the conduction band while losing energy. Since the energy level of the conduction band bottom is higher than that of vacuum, these electrons are also released into the vacuum and a relatively high QE is realized.

GaAs was originally developed for spin polarized electron source at SLAC (Stanford Linear Accelerator Center)[78] in late 1970's. It has been used as polarized electron source for Stanford 2-mile linear accelerator[79] and provided opportunity to study nuclear spin physics[80]. The spin crisis that the sum of the spin content of partons (quark and gluon) are much less than that of nucleon spin, is still one of the hottest issue in the nuclear physics. The polarized electron beam is powerful tool for the particle physics, since each spin state is belong to different category in SU(2) x U(1) gauge interaction[81]. The right handed electron is singlet, but the left handed electron is belong to doublet together with neutrino. If the right handed electron is used for a particle physics experiment, the weak interaction is prohibited. By observing asymmetry of interaction by switching the polarization, we can study the detail of the structure of particle interaction.

SLC[82] which was a first linear collider in the world, was operated on Z_0 pole (90 GeV) at 1990' at SLAC. SLC has greatly contributed to establish the standard model of particle physics, together with LEP at CERN[6]. There is no doubt that the spin polarized electron beam has a crucial role in the next high energy program, ILC, too.

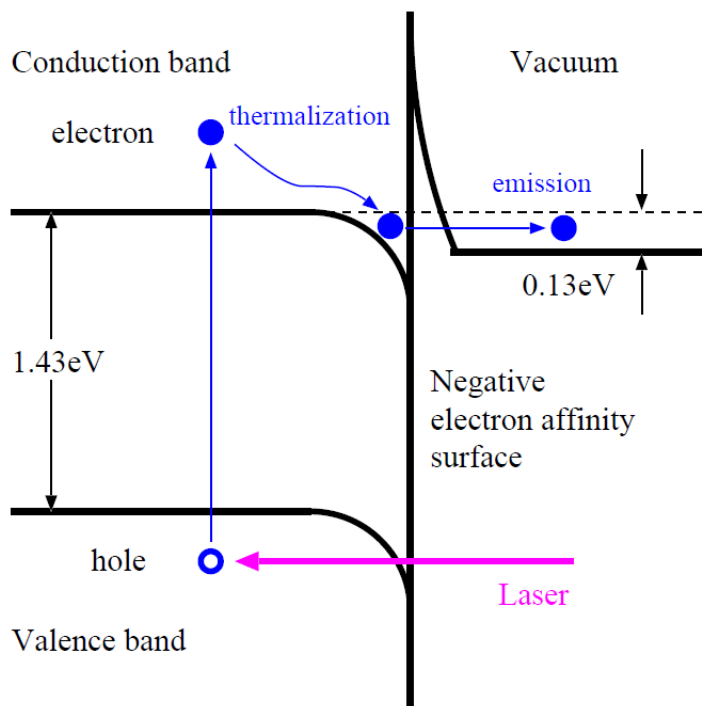


Figure 3.1: Schematic drawing of the photo-electron emission from the NEA GaAs cathode. Electron excited by laser to the conduction band is thermalized. Because the state of the conduction bottom has higher energy than that of the vacuum, electron can be emitted through the surface thin barrier. [20]

The spin polarized electron beam is also useful to study magnetization of material. Spin Polarized Low Energy Electron Microscopy[83] is developed to observe the magnetization.

Spin polarized electron is generated by photo-emission from NEA GaAs with circularly polarized laser corresponding to a band gap energy. Since the excited electron does not have kinetic energy in the conduction band, NEA surface is necessary for photo-electron emission to vacuum. The spin polarized electron emission from NEA-GaAs is explained in the Appendix A for detail.

The polarization is principally limited up to 50% with a bulk-GaAs crystal since it is determined by matrix element of the transition as expressed with Clebsch-Gordon coefficient. By breaking the degeneration of the spin 3/2 valence states,

a specific transition is enhanced giving 90% polarization[84]. There are several techniques to break the degeneration and the strained super-lattice crystal is the state of the art[85]. In ILC[12], the GaAs/GaAsP strained super-lattice crystal is employed as the photo-cathode.

Because the conduction band at the NEA surface is higher than the vacuum, electrons with tiny momentum is extracted to vacuum resulting an extremely small emittance. It is basically possible to obtain such small emittance beam with PEA cathode by adjusting the laser wave length, we have to be patient for small QE. In NEA case, QE is kept high, because electrons with a small momentum are also extracted. NEA GaAs cathode is useful for high brightness (large current and small emittance) electron source[51][86]. On the other hand, because thermalized electrons in the conduction band is extracted to vacuum, the time response of the emission is quite slow, in order of several 10 ps. NEA GaAs is not feasible as the short pulse electron source.

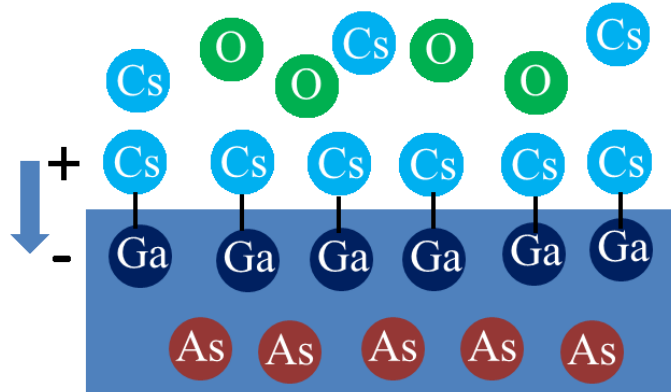


Figure 3.2: A schematic diagram of the electric dipole made by Cs vapor-deposited on the GaAs surface. Electric dipoles are formed on the GaAs surface, and the surface potential is lowered.

In contrast to the large improvement on the spin polarization and the good performance of the beam from the NEA cathode, the structure of the NEA surface is not understood well. The NEA surface is artificially formed by Cs and O₂[87][88] or NF₃[89] evaporation on a cleaned GaAs surface[90] as explained. Figure 3.2 shows a schematic diagram of the electric dipole made by Cs vapor-deposited on the GaAs surface according to the hypothesis. Electric dipoles are formed on the GaAs surface, and the surface potential is lowered. According to an investigation of the NEA surface by STM, the work function of p-GaAs(110) was lowered by Cs adsorption on its surface[91], but the role of Oxygen or NF₃ in the NEA activation has not been understood well. By analyzing spectra of QE of NEA GaAs, it is

suggested that the thickness of the surface potential is decreased by progress of Yo-Yo process[92]. According to an investigation of the NEA surface by X-ray absorption fine structure(XAFS), the structure of the NEA surface may be O-Cs-As(Ga)[93] or Cs-O-As(Ga)[94] with Cs and O₂ activation.

The NEA surface can be easily damaged by residual gas adsorption [95] [96][97] and ion back-bombardment[98][99]. For example, the 1/e lifetime of NEA surface with the average current of 50 μA is only 100 hours with 200 kV electron gun (NPES - 3)[100]. The lifetime is further shortened with a large current extraction. 10% initial QE is degraded to down to less than 1% by 20mA 1.5 h operation[101]. Understanding the NEA surface and improving the cathode robustness are important issues not only from the fundamental physics point view, but also the practical view point.

In Chapter 5, we studied the activation process of NEA surface with several gas(CO₂, CO, and N₂) species to improve our understanding for the NEA surface.

Chapter 4

Substrate dependence of CsK₂Sb cathode

In this chapter, we describe the experiment for the substrate dependence of CsK₂Sb photo-cathode and the analysis. CsK₂Sb cathode was fabricated on Si(100), Si(111), and GaAs(100) and the performance was compared. To observe the dependence significantly, the cathode evaporation condition was optimized at first. For each substrate, the as-received and cleaned surfaces were also compared.

4.1 Experimental Setup

CsK₂Sb cathode is formed on a substrate with evaporation in a vacuum chamber. This evaporation chamber is made from SUS 304 chemically polished on the inner surface. The picture and 3D drawing are shown in Figure 4.1 and Figure 4.2, respectively. The vacuum was maintained with an ion pump (ULVAC PST-100 100 l/s pumping speed)[102] and NEG (Non Evaporative Getter , SAES Capacitorr-D400 480 l/s) [103] and was kept at UHV (a typical pressure was 1.0e-8Pa). The cathode (substrate) is fixed on a puck made from molybdenum and SUS (cathode puck) and the chamber accommodates up to three pucks. Figure 4.3 shows the drawing of the cathode puck.

The puck is mounted on the cathode holder during evaporation and photo-electron emission. Three cathode pucks are placed vertically in line on the holder. The Figure 4.4 shows the picture of the cathode holder. The holder can be moved vertically to adjust the position for evaporation, photo-electron emission, and transfer. For each cathode puck, a 15 mm × 15 mm substrate is placed on a molybdenum base plate. The substrate is soldered on the base with indium and fixed by a tantalum cup. Figure 4.5 shows Si and GaAs substrates and Figure 4.6

shows the substrates mounted on the puck. The substrate is soldered on the the base with indium and fixed by a tantalum cup.



Figure 4.1: The picture of the evaporation chamber. This evaporation chamber is made from SUS 304 chemically polished on the inner surface. The vacuum was maintained with an ion pump (ULVAC PST-100 100 l/s pumping speed)[102] and NEG (Non Evaporative Getter , SAES Capacitorr-D400 480 l/s) [103] and was kept at UHV (a typical pressure was $1.0e-8$ Pa).

The evaporation sources are mounted on a linear stage in the chamber. Figure 4.7 shows the picture of the evaporation sources. The high-purity (99.9999%) Sb beads were resistively heated in a tungsten evaporation basket. The K and Cs sources are dispensers provided by SAES Getters Co., Ltd.[104] . The amount of material on the substrate was monitored with a quartz thickness monitor (INFICON Q-pod Quartz Crystal Monitor). The cross-sectional view of the arrangement around the cathode puck is shown in Figure 4.8. The thickness monitor is placed in a symmetrical position to the cathode substrate in order to absorb an equivalent amount of vapor. The source to substrate distance was maintained at about 12 mm during the evaporation. To control the cathode temperature, a tungsten heater is used. The heater is mounted on the head of the linear mover, which can be inserted from back side of the cathode puck, as shown in Figure 4.8. The

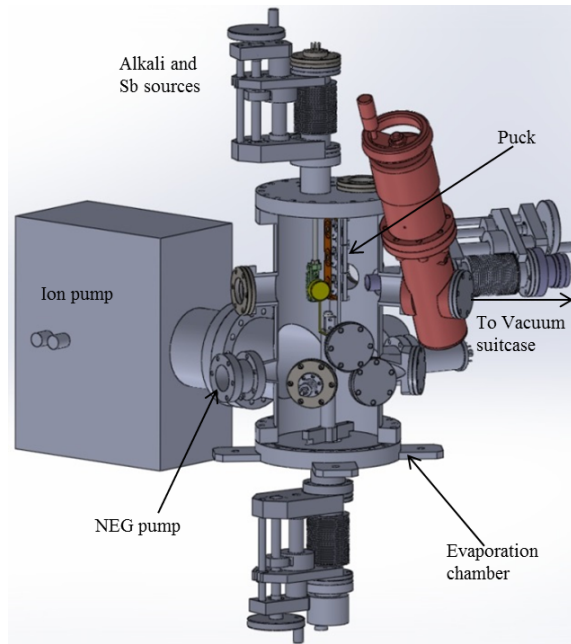


Figure 4.2: 3D drawing of the CsK_2Sb evaporation chamber. Up to 3 cathode pucks can be stored in the chamber. The cathode can be transferred through the gate valve to another vacuum chamber (vacuum suitcase) for cathode transportation.

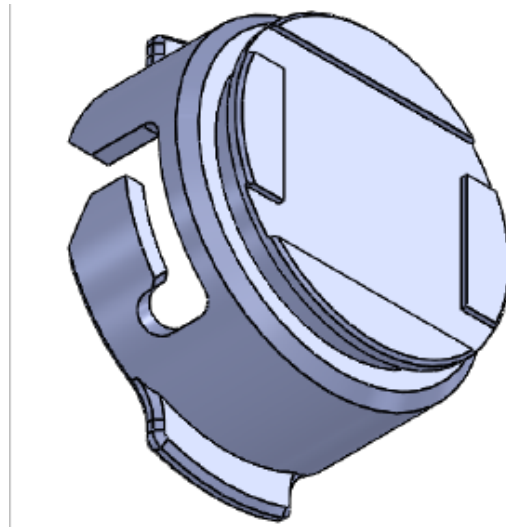


Figure 4.3: The drawing of the cathode puck. For each cathode puck, a 15 mm \times 15 mm substrate is placed on a molybdenum base plate.

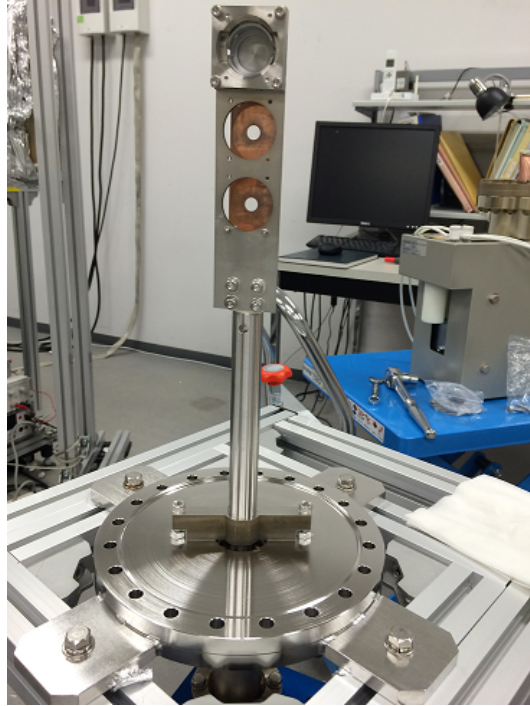


Figure 4.4: The picture of the cathode holder. Up to 3 cathode pucks can be set. The holder can be moved vertically to adjust the position for evaporation, photo-electron emission, and transfer.

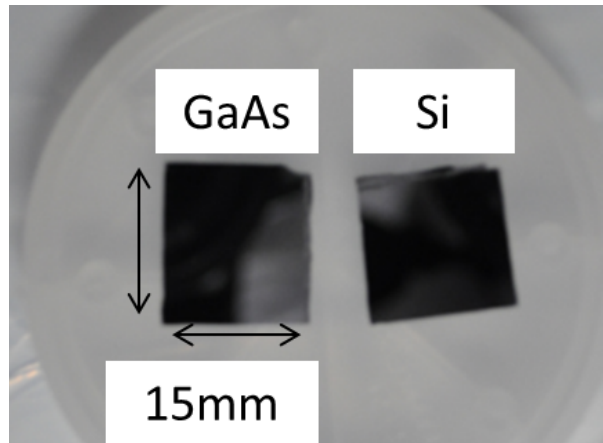


Figure 4.5: Si(100) and GaAs(100) substrates. Si(100) and Si(111) wafers with a $\leq 0.002 \Omega\text{cm}^{-1}$ and GaAs(100) p-type wafer are employed as the substrates.

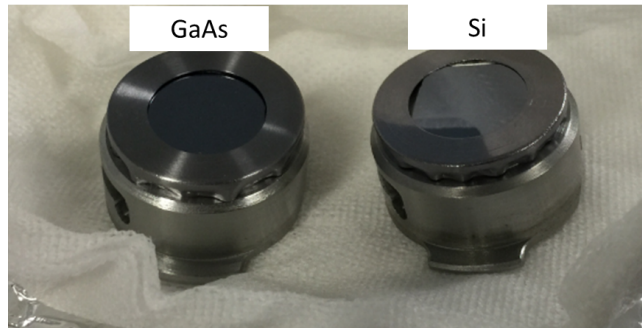


Figure 4.6: The substrates mounted on the puck. The substrate is soldered on the the base with indium and fixed by a tantalum cup. The puck is mounted on the cathode holder during evaporation and photo-electron emission.

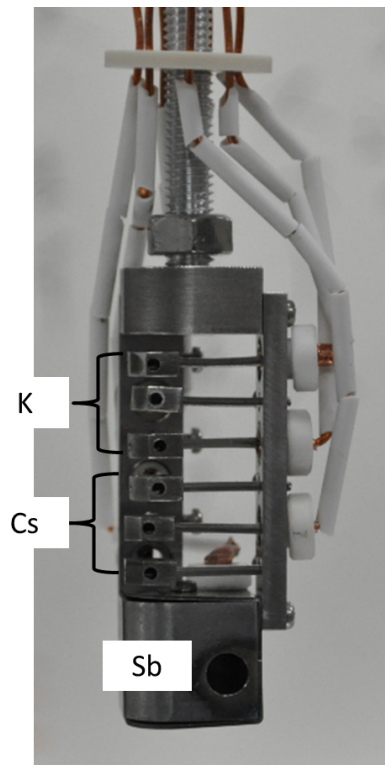


Figure 4.7: The picture of the evaporation sources. The evaporation sources are mounted on a linear stage in the chamber. K and Cs can be set each of three in the evaporation sources. The Sb pellets were resistively heated in a tungsten evaporation basket.

cathode puck temperature is measured with a thermocouple.

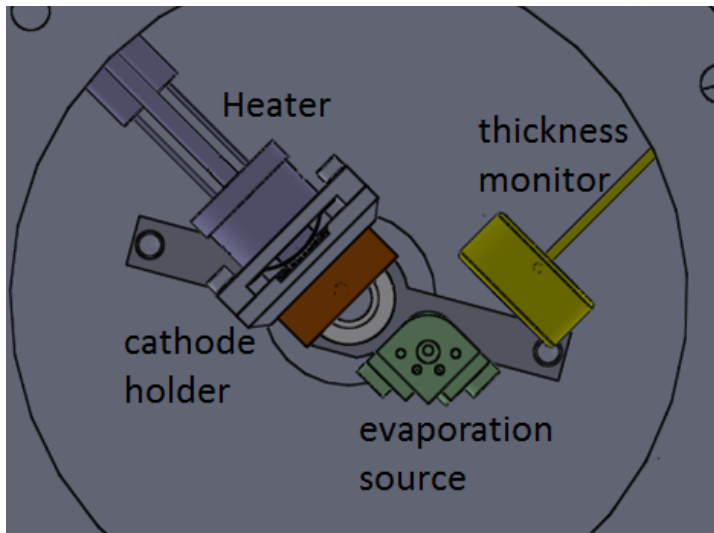


Figure 4.8: A vertical view of the arrangement around the cathode puck. The thickness monitor and the cathode puck were placed in symmetrical positions to the evaporation source. The cathode puck temperature is controlled by a heater from the backside.

The QE was measured with a 532 nm laser. The 1.0 mW light of 532 nm emitted from laser transmits through the ND - filter for laser power adjustment. In fact, it is possible to install multiple ND filters, and the power is adjusted to 20 to 500 μ W. A manual shutter controls the irradiation to the cathode. A simple 2D scan can be taken with a manual stage. The cathode was biased at -100 V, and the photo-current was measured as the current of the bias supplier.

4.2 Substrate surface treatment

According to previous studies[25][72][105], the QE depends strongly on the substrate surface state, i.e., oxidation, roughness, etc. In this study, Si(100) and Si(111) p-type wafers with a resistivity of $\leq 0.002 \Omega\text{cm}^{-1}$ and GaAs(100) p-type wafers are employed as the substrates. Si wafer was etched, single side polished and finally washed with RCA method by NILACO Co. Ltd. GaAs wafer was etched, double-side polished, and finally washed with RCA method, as well. These substrate surfaces were oxidized again because it was treated in air. To control the surface state of the substrate, we perform the etching of the substrate sample prior to the experiment as follows.

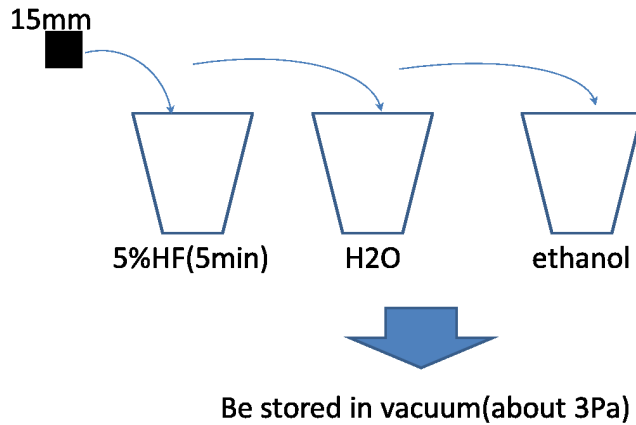


Figure 4.9: Etching procedure of Si substrate. The Si(100) and Si(111) substrates were processed with a 5% HF solution for about 5 min.[106]

The Si(100) and Si(111) substrates were processed with a 5% HF solution for about 5 min to remove the surface oxidized layer[106] as the process shown in Figure 4.9. The GaAs surface was processed with a H₂SO₄:H₂O₂:H₂O (4:1:1) solution for about 1 min to remove the surface oxidized layer[90] and to make As rich surface. The As layer is removed by heating in the vacuum chamber to obtain the clean GaAs surface. The process is called as heat cleaning. The process is shown in Figure 4.10.

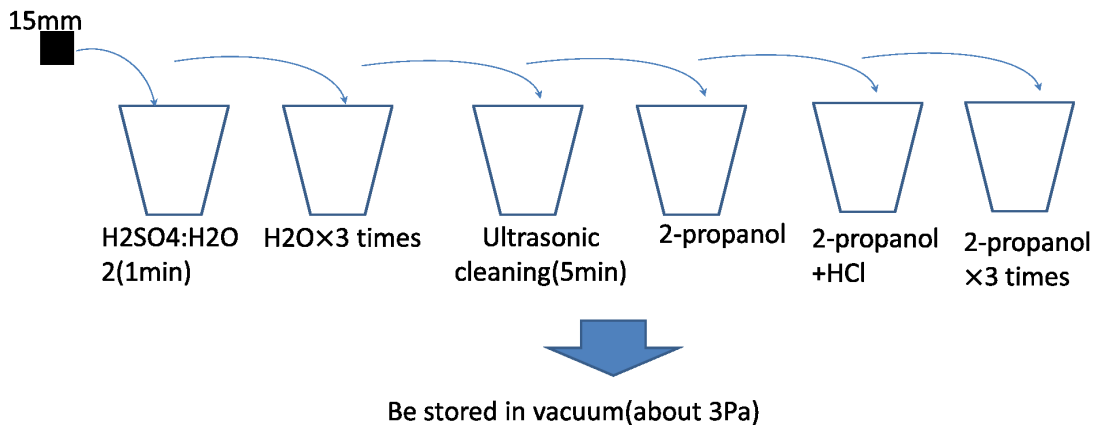


Figure 4.10: Etching procedure of GaAs substrate. The GaAs surface was processed with a H₂SO₄:H₂O₂:H₂O (4:1:1) solution for about 1 min[90] and to make As rich surface.

According Ref.[106] , the surfaces of Si(100) and Si(111) are equivalent except

the surface direction after the HF treatment. This cleaned surface is kept for 3 and 50 hours in air for Si(100) and Si(111), respectively [107]. In our experiment, after the cleaning, the Si sample was kept in a desiccator (typical pressure was 3Pa) and the air exposure duration during the sample transfer was totally less than 30 minutes and the re-oxidation on the substrates are negligible. Therefore, the Si(100) and Si(111) substrates in our experiment are kept clean and are equivalent except the surface atomic arrangement.

To examine the effect of the surface oxidation, we perform the cathode evaporation also on the as-received substrates[108][109]. The atomic arrangement of the as-received surface is disturbed by the oxidation layer[110], and it is considered to be amorphous[109][110]. That could be also true for GaAs.

4.3 Experimental Results

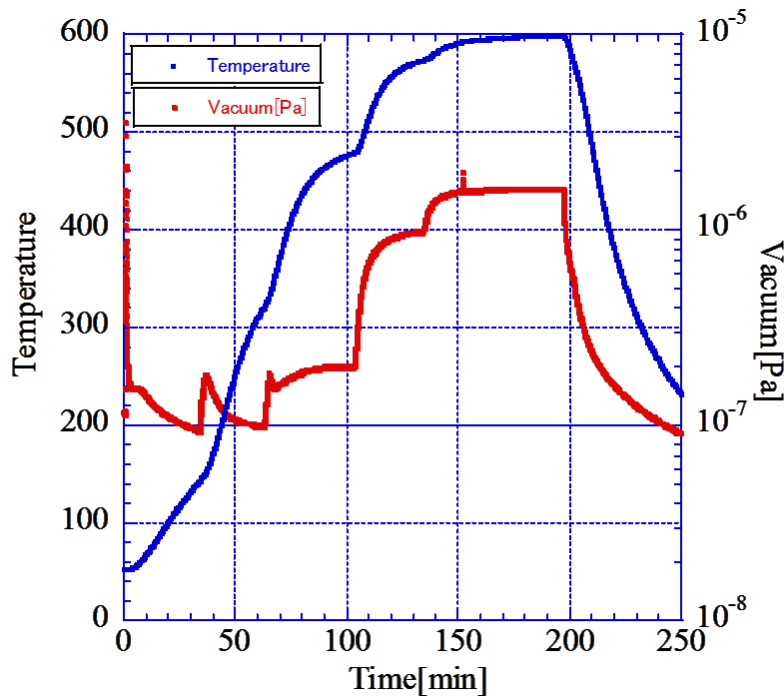


Figure 4.11: Heat cleaning. The substrate is heated up to 600°C in vacuum. Temperature is shown red line and vacuum pressure is shown blue line during the heat cleaning.

Before the evaporation, in order to remove impurities on the substrate surface, we perform the heat cleaning. The substrate is heated up to 450–600°C in vacuum. This process is performed not only for a virgin substrate which was newly installed

to the experimental chamber, but also for an used substrate. In every cathode evaporation, we perform the process. Figure 4.11 shows temperature (red line) and vacuum pressure (blue line) evolutions during the heat cleaning.

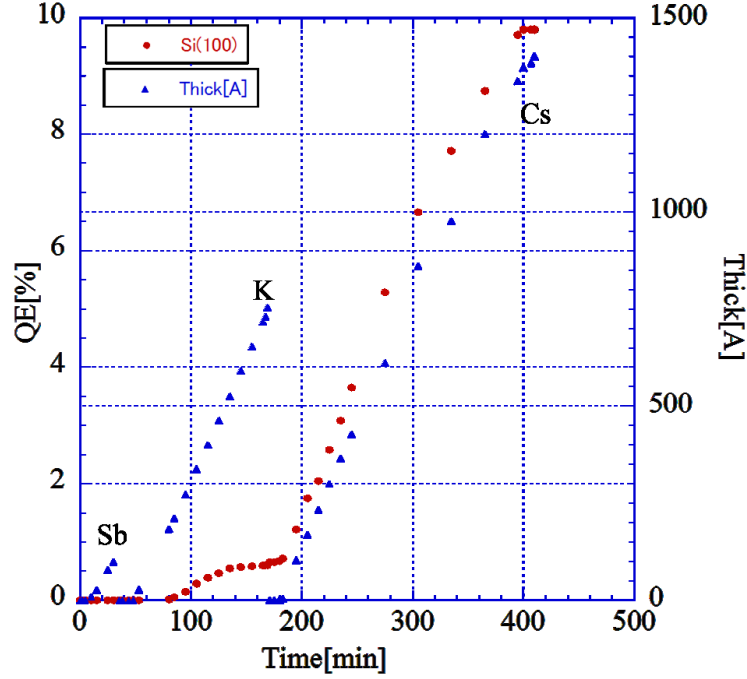


Figure 4.12: QE evolution and progress of thickness of Sb, K, and Cs. QE evolution is shown red circle and progress of thicknesses of Sb, K, and Cs are shown blue triangle. QE appears in K evaporation and increases rapidly in Cs evaporation. The thickness are 10nm, 70nm and 1400nm for Sb, K and Cs, respectively.

CsK₂Sb cathode was formed by sequential evaporation of Sb, K, and Cs on a substrate. The evaporation procedure is summarized as follows:

1. Heat cleaning.
2. The temperature is lowered down to 100°C. This temperature was maintained during the evaporation.
3. A 10-nm-thick layer of Sb is evaporated on the substrate surface.
4. K is evaporated. Simultaneously, QE is observed by illuminating the cathode with 532-nm laser light. The evaporation is stopped when QE is saturated, which usually occurs between 0.3–0.8%. The typical thickness of K was 60 nm.

5. The Cs layer is evaporated. The Cs evaporation is controlled with the same manner as that for the K evaporation. The QE was typically between 1–10% and the thickness was 140 nm.
6. The substrate is cooled down to room temperature.

Figure 4.12 shows an example of QE evolution with red circle and progress of thicknesses of Sb, K, and Cs with blue triangle. The laser power was adjusted to 0.8mW during the K evaporation and 0.36mW during the Cs evaporation to avoid the space charge limitation. The laser spot size was 0.5 mm^2 , and the typical photo-current was $1 - 3 \mu\text{A}$ for K evaporation and $3 - 9 \mu\text{A}$ for Cs evaporation.

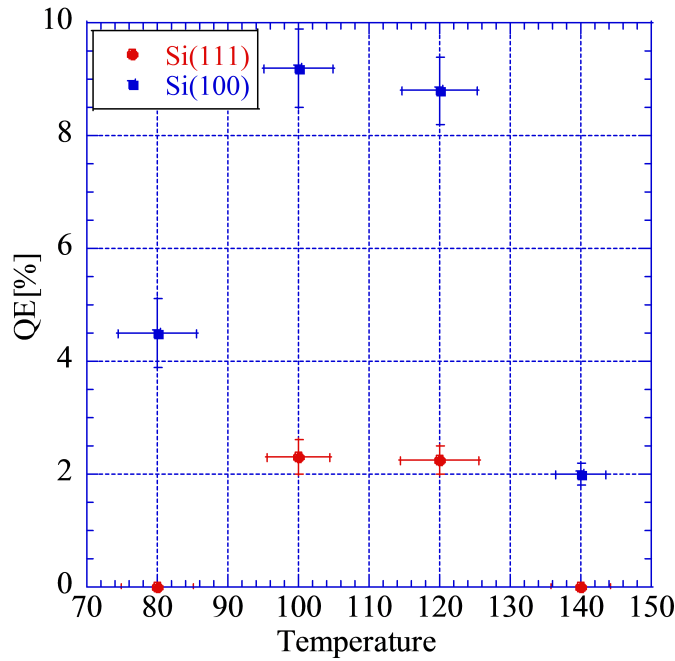


Figure 4.13: The maximum QE is shown as a function of temperature during the evaporation with blue squares and red circles for the Si(100) and Si(111) substrates, respectively. The error on the horizontal axis is fluctuation during evaporation and the error on the vertical axis is statistical error by 3 times measurements.

QE of CsK_2Sb depend on the evaporation condition even the substrate is same [74]. In order to eliminate such effect, we fixed the evaporation condition (Sb thickness and substrate temperature during the evaporation) giving a maximum QE and less QE fluctuation regarding to condition variation. Amount of K and Cs were automatically determined giving the maximum QE after each evaporations. The maximum QE of CsK_2Sb as a function of substrate temperature is shown

in Figure 4.13 for Si(100) and Si(111) substrates, respectively. We repeated the evaporation several times for each substrates. The error on the horizontal axis is temperature fluctuation during Cs evaporation and error on the vertical axis is statistical error. We found that QE is maximized around 100°C on Si(100) and Si(111) with a good reproducibility. Figure 4.14 shows that the QE as a function of Sb thickness showing a weak dependence.

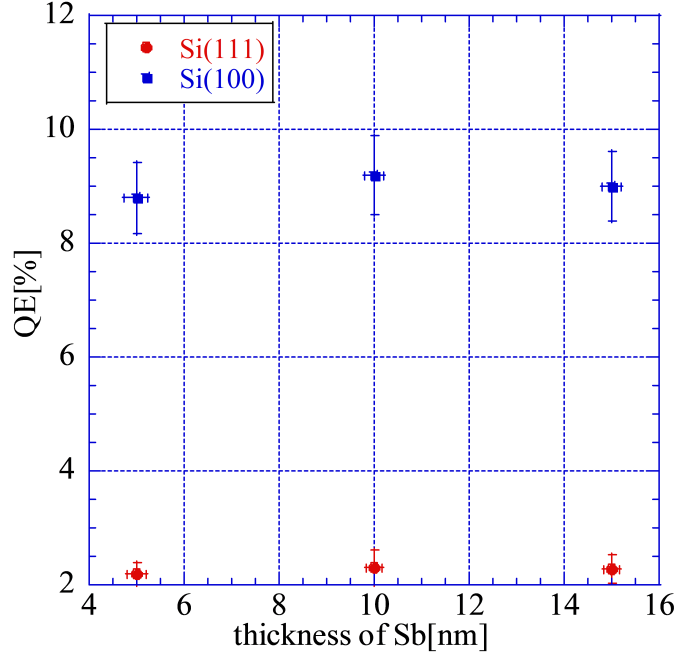


Figure 4.14: The maximum QE is shown as a function of Sb thickness with blue squares and red circles for the Si(100) and Si(111) substrates, respectively. The error on the horizontal axis and error on the vertical axis are only statistic.

According to these results, the evaporation was performed at 100°C with 10 nm Sb thickness. Amount of K and Cs are automatically determined to maximize QE after each evaporation, i.e. we stopped the evaporation whenever QE is saturated.

We examined Si(100), Si(111), and GaAs(100) substrates. The comparison of QE evolution during the cathode evaporation is shown in Figure 4.15 for the cleaned substrates and Figure 4.16 for the as-received substrates. Figure 4.15 shows red circles, blue triangles, and green squares for the cleaned Si(100), Si(111), and GaAs(100) substrates, respectively. QE appears in K evaporation and increases rapidly in Cs evaporation. K evaporation started on 48, 45 and 45 min for the cleaned Si(100), Si(111), and GaAs(100) substrates, respectively. Cs evaporation started on 183, 175 and 135 min for the cleaned Si(100), Si(111), and GaAs(100) substrates, respectively. Figure 4.16 shows that the comparison of QE evolution

during the cathode evaporation is shown with red circles, blue circles, and green circles for the as-received Si(100), Si(111), and GaAs(100) substrates, respectively. In the blue, green, and yellow shaded regions, Sb, K, and Cs were evaporated, respectively. The QE appears in the K evaporation and increases rapidly in the Cs evaporation.

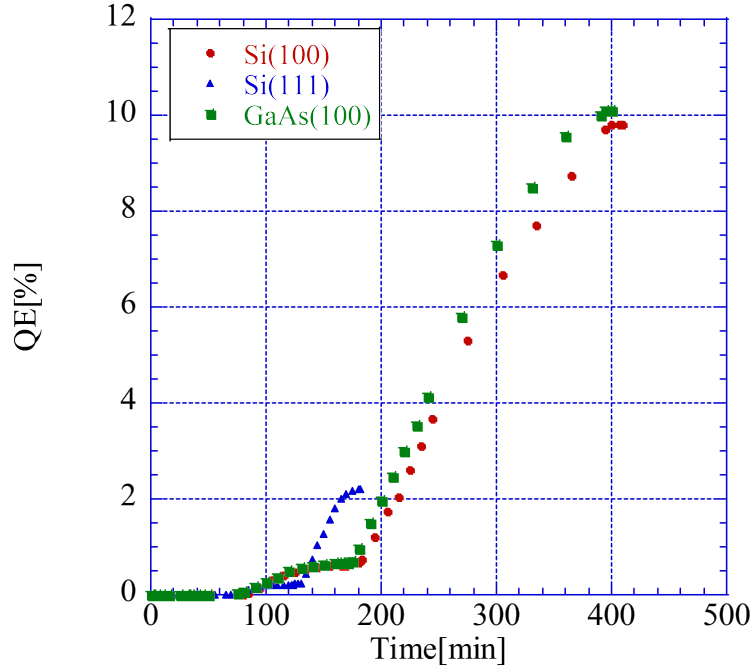


Figure 4.15: The comparison of QE evolution during the cathode evaporation for the cleaned substrates are shown with red circles, blue triangles, and green squares for the cleaned Si(100), Si(111), and GaAs(100) substrates, respectively. QE appears in K evaporation and increases rapidly in Cs evaporation. K evaporation started on 48, 45 and 45 min for the cleaned Si(100), Si(111), and GaAs(100) substrates, respectively. Cs evaporation started on 183, 175 and 135 min for the cleaned Si(100), Si(111), and GaAs(100) substrates, respectively.

The results (maximum QE) are summarized in Table 5.1 including the those of preceding studies. We performed the same experiment five times for each substrate. After every experiment, the substrate was heat-cleaned to initialize the surface. The error is obtained as the standard deviation of the five measurements, and it is statistical only. The QE of the as-received substrate was around 2.5–5.5% at 532 nm. The cleaned Si (100) and GaAs(100) substrates showed a good QE as high as 10%. These results are similar to those of the cleaned Mo(100)[25] and Si(100) substrates obtained by Cornell University[26]. In contrast, the QE of the cleaned Si(111) was higher than that of the as-received Si(111), but it is much lower than

that of the cleaned Si(100) and GaAs(100) substrates.

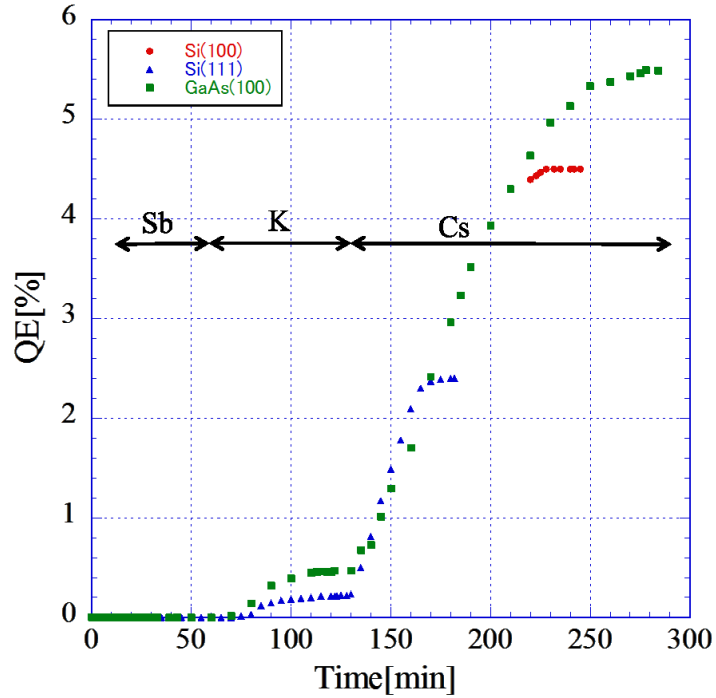


Figure 4.16: The comparison of QE evolution during the cathode evaporation is shown with red circles, blue circles, and green circles for the as-received Si(100), Si(111), and GaAs(100) substrates, respectively. In the blue, green, and yellow shaded regions, Sb, K, and Cs were evaporated, respectively. The QE appears in the K evaporation and increases rapidly in the Cs evaporation.

According to results shown in Table 5.1, the cathode performance developed on the cleaned substrate was significantly higher than that on the as-received substrate for all cases. The cathode formed on the Si(111) substrate showed the least performance in the sample substrates in both the cleaned and as-received cases. The difference in the cathode performance on the Si(100) and Si(111) substrates provide direct evidence that the cathode performance depends strongly on the surface direction, because the material properties of Si(100) and Si(111) are exactly the same otherwise. A similar conclusion was also obtained by comparing QE of the crystalline Mo(100)[25] and amorphous Mo[29][31], because the physical properties of the crystalline and amorphous Mo other than the surface atomic arrangements, are almost the same. Mo(100) and Mo(amorphous) substrates in Reference [25][29][31] are considered to be cleaned because they were polished and sputtered.

The results can be summarized as

- By comparing the as-received and cleaned substrates, the cathode on the

Table 4.1: The maximum QE of the CsK₂Sb photo-cathode on Mo(100), Mo(amorphous), Si(100), Si (111), and GaAs (100) substrates at 532 nm are summarized.

Substrate	Surface treatment	QE[%]@532nm
Mo(100)	Polished+sputter	10.0[25]
Mo(amorphous)	Polished+sputter	2-5[29][31]
Si(100)	as-received	4.8 ± 0.6
Si(100)	5%HF	9.4 ± 0.7
Si(100)	5%HF	7 – 10[26]
Si(111)	as-received	1.6 ± 0.1
Si(111)	5%HF	2.3 ± 0.3
GaAs(100)	as-received	5.5 ± 0.2
GaAs(100)	H ₂ SO ₄ :H ₂ O ₂ :H ₂ O	10.0 ± 0.2

cleaned substrates shows better performance.

- By comparing amorphous and crystalline substrates, the cathode on the crystalline substrates shows better performance.
- By comparing Si(100) and Si(111), the cathode on Si(100) shows better performance.

By considering these facts, the cathode performance depends not only on cleanliness and crystallinity, but also on surface direction of the crystalline substrate. This is the first experimental evidence that CsK₂Sb cathode performance depends on the crystal surface direction of the substrate. In the following section, we discuss these results.

4.4 Discussion

CsK₂Sb forms a DO₃ cubic structure [63][65] as explained already. Figure 4.17 and Figure 4.18 shows that the surface atomic arrangements of CsK₂Sb(100), CsK₂Sb(111), Mo(100), GaAs(100), Si(100), and Si(111) surfaces. By considering the matching between the atomic arrangements among CsK₂Sb (100), (111), Si(100), Mo(100), and GaAs(100) surfaces, CsK₂Sb are grown in (100) direction on Si(100), Mo(100), and GaAs(100) surfaces, and in (111) direction on Si(111) direction. Atomic arrangement model of unit cell is explained in the Appendix B for detail.

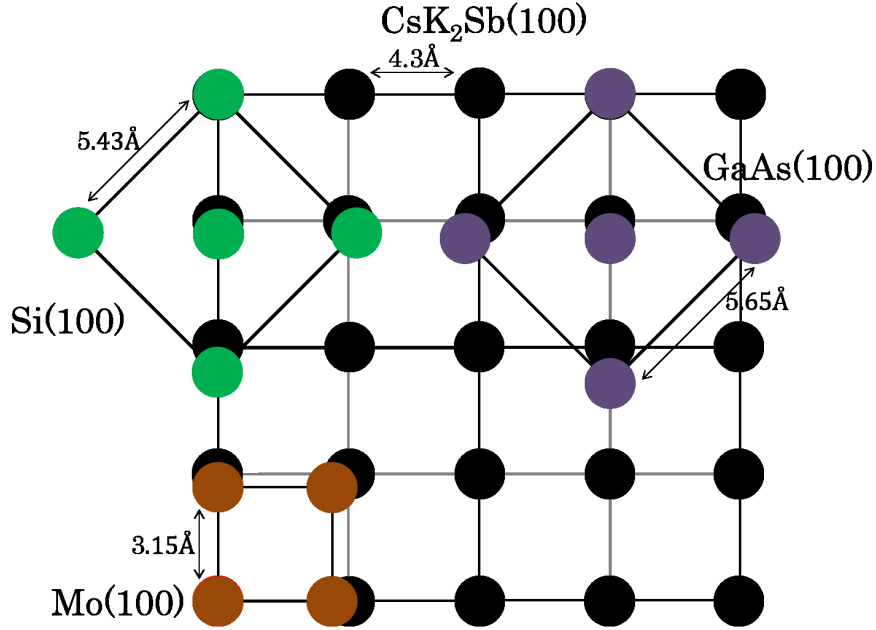


Figure 4.17: Atomic arrangement of CsK₂Sb(100) on the Mo(100), GaAs(100) and Si(100) surfaces. The lattice constants of Mo, Si, and GaAs are 3.15Å, 5.43Å, and 5.65Å, respectively [111].

The reason for the reduced performance of the as-received substrates comparing to the cleaned substrates could be the less quality of CsK₂Sb crystal. Oxidation distorts the atomic arrangement of the substrate surface resulting a poor quality of CsK₂Sb crystals leading the reduced performance.

The cathode on the cleaned Si (100) and GaAs(100) substrates showed a good QE as high as 10%. These results are similar to those on the cleaned Mo(100) and Si(100) substrates obtained by the Cornell University[25]. On the other hand, the cathode performance on Si (111) is less than the others. These results can be explained with the band structure of CsK₂Sb. In References [63][65], the bulk band dispersion of CsK₂Sb was calculated. The point on the boundary surface of the Brillouin region is called the K, L, and X points in the (110), (111), and (100) directions, respectively. According to the bulk band dispersion, CsK₂Sb is a direct transition type at the Γ point with 1.1 eV bandgap. The bandgap is about 2.1, 3.1, and 1.4eV at K, L, and X points, respectively. If we consider the photo-electron emission in (100) direction, not only electrons at Γ point, but also electrons at X point contributes to the emission, because the bandgap at X point is similar to that at Γ . On the other hand, for the photo-electron emission in (111) direction, there is no contribution at L point, because the bandgap energy (3.1 eV) is larger

than the laser photon energy (2.3 eV at 532 nm). The photo-electron emission of CsK₂Sb in (111) direction is possible only at Γ point and this is the reason why the QE of (111) surface is less than that of (100) surface.

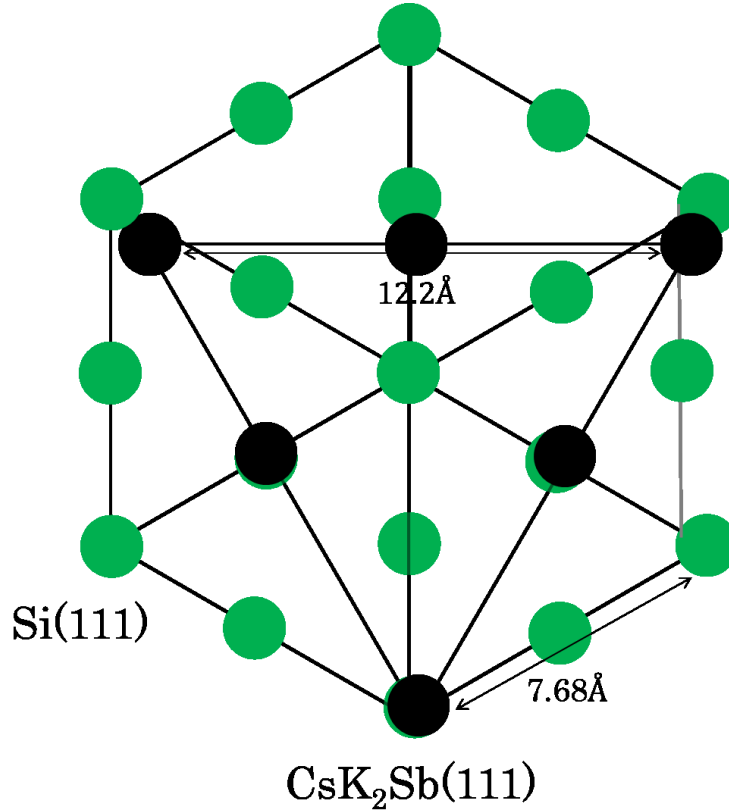


Figure 4.18: Atomic arrangement of CsK₂Sb(111) on the Si(111) surface.

By a similar consideration, the QE of (110) surface should be less than that of (100) surface. In the preceding studies[74][75], CsK₂Sb was grown in (200) or (220) directions on Si (100) substrate, depending on the case and the cathode performance of (200) and (220) were similar[74]. We consider that the cathode evaporation conditions in these experiments were not fully optimized, because the QE is only 3% for 532 nm light in both cases. That is why CsK₂Sb crystal direction depends on the case and there was no significant difference on the cathode performance grown in (100) and (110) directions in these studies.

In our case, the cathode evaporation condition was carefully optimized and the cathode performance reproducibility was quite good. The cathode performance dependence on the substrate crystallinity and the surface direction was confirmed based on the reliable experiments.

Chapter 5

Effect of Gas Adsorption on NEA GaAs

To improve our understanding for the NEA surface, we studied the activation process of NEA surface. In this study, we activated the NEA surface of GaAs with different gas species and compared the cathode performance. We examined CO₂, CO, and N₂ as test gases and compared them with O₂. In this chapter, we describe the experiment followed by the results and discussion.

5.1 Experimental Setup

NEA activation experiments were carried out with a test chamber described in Ref. [112]. The vacuum was maintained with a 160 l/s ion pump and 310 l/s non-evaporative getter (NEG) pump and was kept at ultra-high vacuum (UHV). The typical pressure was 6.0×10^{-9} Pa. The chamber is made from SUS and the inner surface was finished by chemical polishing.

1.0-inch GaAs wafer is cut to 4 pieces. One piece is placed on a molybdenum base plate. It is soldered on the base with indium and fixed by a tantalum cup. In this study, the p-type, Zn-doped bulk GaAs(100) was used as a cathode sample. The doping density is $4.0 \times 10^{19} \text{cm}^{-3}$. This high doping causes the band bending at the surface, which lowers the effective work function. The GaAs surface was processed with a H₂SO₄:H₂O₂:H₂O (4:1:1) solution for about 1 min to remove the surface oxidized layer[90] as same as substrate process in Chap. 4. The temperature of the cathode mount can be controlled with a tungsten heater embedded in the mount. The GaAs cathode temperature is measured with a thermocouple attached to the cathode mount.

The sample gas introduction system is shown in Figure 5.1. To provide several

sample gas species, three gas cylinders are connected to a leak valve attached to the main chamber. The gas species can be switched by toggling several valves. To avoid mixture of undesired gas species, the sample gas introduction system is evacuated by a rough pump (molecular pump) while every switching.

A quadrupole mass spectrometer, QMS (M101QA-TDM-W, ANELVA) is used for the gas analysis. The sample gas contains not only the specific molecule, but also fragment components and contaminations. The gas content is obtained by analyzing the mass-to-charge ratio (m/z) spectrum up to 100 m/z measured by QMS.

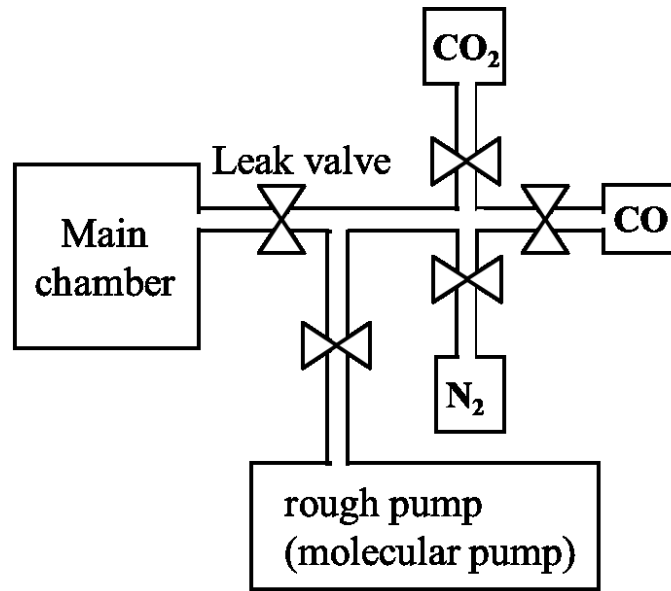


Figure 5.1: A schematically drawing of the sample gas introduction system. The system and the main chamber are connected by a leak valve to control the gas introduction rate. The gas species can be changed by toggling valves to each gas bombs. The system is evacuated by a rough pump for every gas switching to avoid gas mixture.

5.2 Experimental Results

The NEA GaAs cathode was formed by alternate evaporations of Cs and gas (O_2 as reference) on a cleaned GaAs substrate (yo-yo method)[113]. The procedure is given as follows:

1. The GaAs substrate is heated to 600°C and held at that temperature for one hour to clean the surface (heat cleaning process).

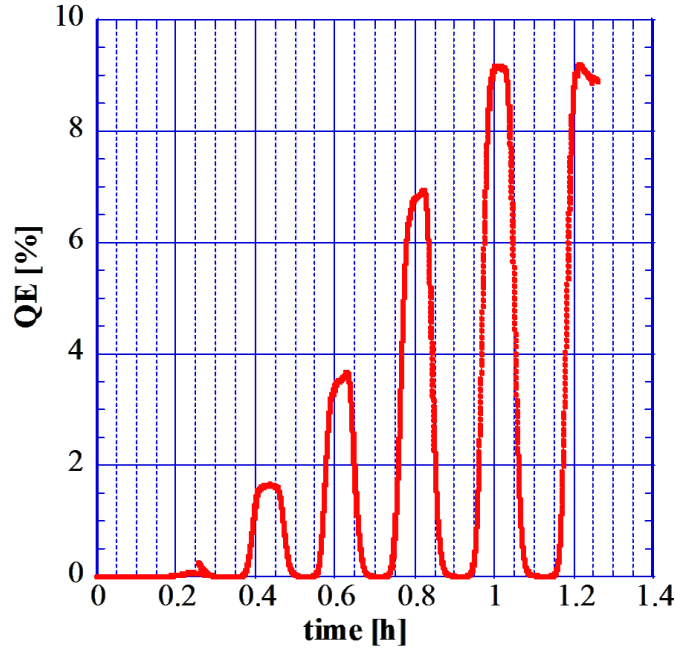


Figure 5.2: QE evolution during the activation process by Cs and O₂. The first peak is made by Cs only. In other peaks, QE is increased by O₂ and decreased by Cs.

2. The GaAs wafer is cooled down to the room temperature.
3. Cs is evaporated on the GaAs. Usually, a small enhancement of QE is observed, but it is shortly disappeared (Cs peak).
4. Gas (O₂ or NF₃) introduction and Cs evaporation are alternately performed on the GaAs. In a usual activation process, QE is increased when the gas is applied, but it is saturated at some moment. We switched to Cs evaporation and QE is rapidly decreased down to zero. This process is repeated whenever the height of the peak is increased.

QE is simultaneously observed by illuminating the cathode with 633nm He-Ne laser. We examined CO₂, CO and N₂ as the test gas. Addition to these gas species, O₂ was used as the reference. The QE evolutions during the NEA activation with O₂, CO₂, CO and N₂ are shown in Figures 5.2-5.5, respectively.

Figure 5.2 shows the QE evolution of the NEA activation with O₂ gas. The first peak is made by Cs evaporation. In other peaks, QE is increased by O₂ and decreased by Cs. If the height of the peak is almost same as that of the previous peak, as the sixth peak in Figure 5.2, we terminate the NEA activation process.

Figure 5.3 shows the QE evolution of an activation with CO₂. The first peak

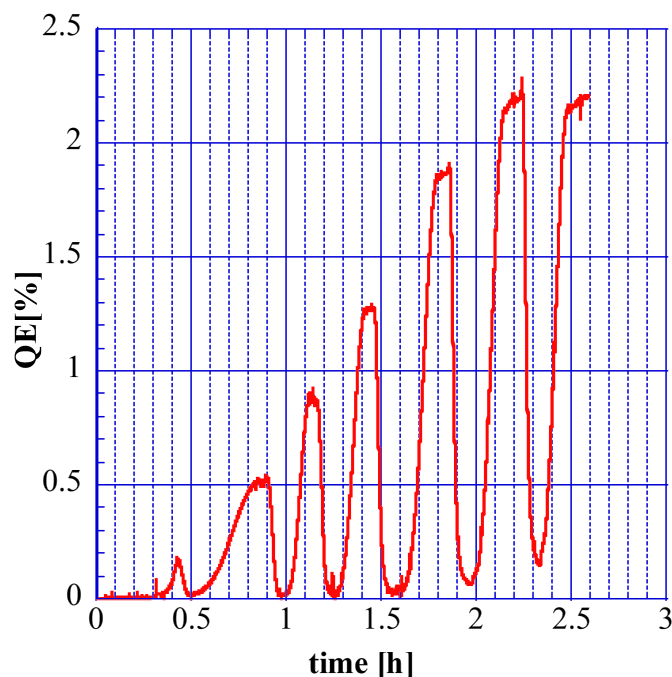


Figure 5.3: QE evolution of the activation process with Cs and CO₂. The activation procedure was same as that with O₂ except the introduced gas.

is made by Cs evaporation. In other peaks, QE is increased by CO₂ and decreased by Cs. The evolution is similar to that with O₂, but the maximum QE value is about 2.3% which is significantly lower than that with O₂.

Figure 5.4 shows the QE evolution of an activation with CO. After the first peak was made by Cs, CO gas was introduced up to $t=0.8$ h, but nothing happened, i.e. QE was not increased at all. CO did not activate GaAs cathode. To confirm the health of the GaAs sample and effect of CO on GaAs, O₂ gas was introduced after $t=0.9$ h, i.e. the usual NEA activation was performed. In Figure 5.4, QE evolutions of the NEA activation with CO and O₂ are drawn with a solid line and a dashed line, respectively. By introducing O₂ gas, QE was increased as same as the usual NEA activation with O₂ and the final maximum QE was more than 9% which is almost same as that in Figure 5.2. From this result, we can conclude that the GaAs sample was healthy (there was no trouble on the preparation) and CO does not activate GaAs cathode. CO gas introduction prior to the process does not disturb NEA activation with O₂, because the NEA surface was activated with O₂ even after CO gas was applied.

Figure 5.5 shows the QE evolution of an activation with N₂. After the first peak by Cs, N₂ gas was introduced up to $t=0.95$ h, but N₂ gas did not activate GaAs cathode at all, as same as that with CO gas. A nominal NEA activation with O₂

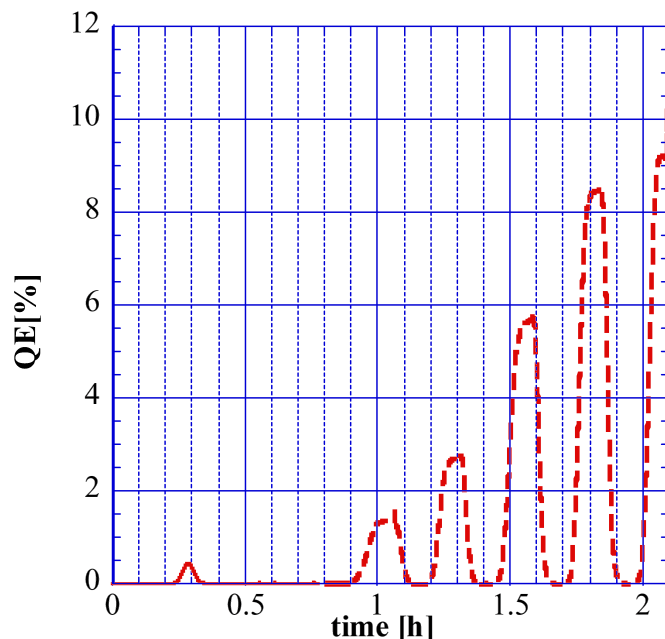


Figure 5.4: QE evolution during the activation process with Cs and CO. QE did not rise with CO. After $t=0.9$ h, the NEA activation was performed by Cs and O_2 . The solid line is that with CO gas introduction and the dashed line is that by O_2 .

gas was performed after $t=1.05$ h and the cathode was activated as same as the nominal NEA activation with O_2 . In Figure 5.5, QE evolutions of the activations with N_2 and O_2 are drawn with a solid line and a dashed line, respectively. From these experiments with CO and N_2 , we suggest that CO and N_2 are not adsorbed on the surface of Cs-GaAs. Even CO or N_2 are introduced in advance, NEA activation with Cs and O_2 is not disturbed, as long as the partial pressure of CO and N_2 is even low during the activation.

5.3 Discussion

Here we consider the difference of the NEA activation with O_2 and CO_2 . It is known that when oxygen atoms or molecules are adsorbed on the Cs-GaAs surface, they accept electrons from Cs atoms and are chemisorbed inside the activation layer forming the NEA surface[114].

Figure 5.6 shows the height of each peak in the Figure 5.2 (NEA activation with O_2) as a function of exposure of O_2 gas in Langmuir ($1L = 1.33 \times 10^{-4} Pa \cdot s$). According to the result, the height is linearly increased as the O_2 gas exposure. Figure 5.7 shows the height of each peak in the Figure 5.3 (NEA activation with

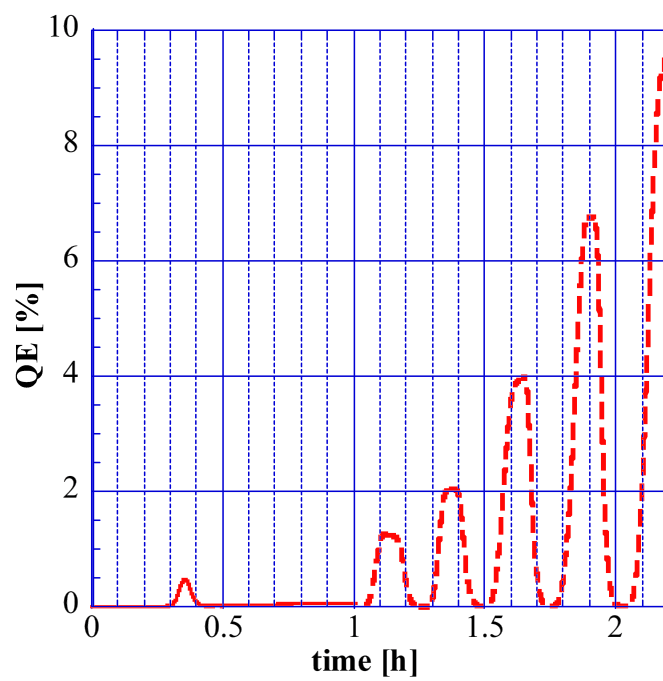


Figure 5.5: QE evolution of the activation process with Cs and N₂. After t=1.05 h, the NEA activation was performed with Cs and O₂. The solid line is that with N₂ gas introduction and the dashed line is that with O₂.

CO₂) as a function of exposure of CO₂ gas. It is quite different from Figure 5.6. The QE height in Figure 5.6 is proportional to the exposure of O₂, but the relation of that with CO₂ in Figure 5.7 is not linear.

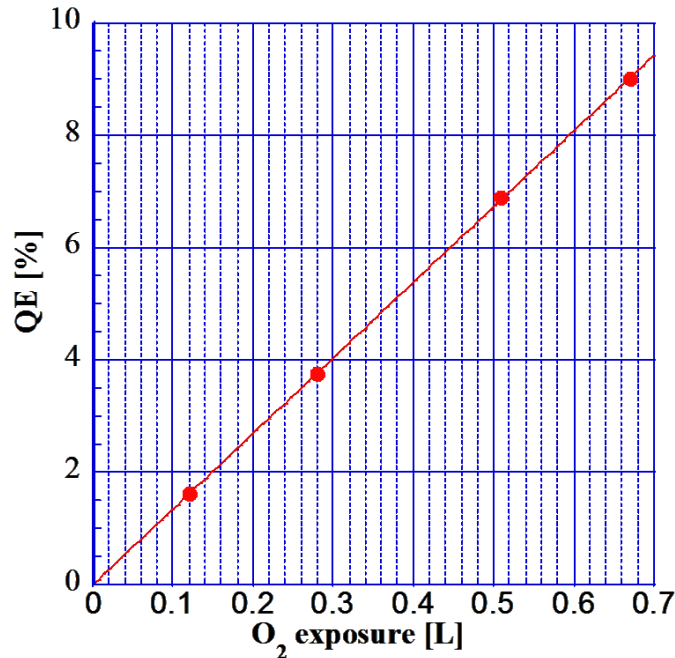


Figure 5.6: The height of each peak in Fig.5.2 is shown as a function of O₂ gas exposure. The red solid line is a fitting curve by assuming Eq. (5.4).

According to our experiment of NEA activation with CO, CO molecule does not contribute to the NEA activation and does not disturb the NEA activation process. On the other hand, CO degrades the NEA GaAs activated with O₂ (nominal NEA activation process), according to Ref. [115]. By considering this degradation effect of CO molecule, the saturation observed in Figure 5.7, i.e. less QE of the NEA GaAs activated with CO₂ can be explained. Because a fraction of CO₂ molecule fragments to CO and O (atomic oxygen), we assume that O (atomic oxygen) activates the NEA surface and CO degrades the activated NEA surface, simultaneously. The QE(η) evolution can be expressed as

$$\frac{d\eta}{dt} = \alpha_1 f_1 - \beta f_3 \eta \quad (5.1)$$

where f_1 is the partial pressure of atomic oxygen, f_3 is the partial pressure of CO, α_1 is the activation ability and β is the degradation ability. The first term of RHS shows activation by atomic oxygen, and the second term shows degradation by CO. We assume the ratio of f_1 and f_3 is constant during experiment as $\mu f_3 = f_1$.

Table 5.1: Mass to charge ratio and ion current of the major peaks of the mass spectrum by QMS with CO₂ introduction. The rightest row shows the candidate molecule. The inside of the parenthesis is the mother molecule.

m/z	Ion current[A]	Molecule daughter (mother)
12	3.32e-11	C(CO ₂), C(CO)
14	3.98e-11	N(N ₂)
16	9.00e-11	O, O(CO ₂), O(CO)
28	7.27e-10	CO(CO ₂), N ₂ , CO
44	4.81e-10	CO ₂

It leads

$$\frac{d\eta}{dt} = \alpha_1 \mu f_3 - \beta f_3 \eta \quad (5.2)$$

We got a solution with $\eta=0$ at $t=0$ as,

$$\eta = \frac{\alpha_1 \mu}{\beta} [1 - \exp(-\beta x_3)], \quad (5.3)$$

where $x_3 = \int_0^t f_3 dt$, i.e. exposure of CO. This model can explain not only the lower QE of the activation with CO₂ than that with O₂, but also the non-linearity of the curve in Figure 5.7 as we will see soon.

The content of CO₂, CO, and atomic oxygen in the experimental chamber were measured with QMS. The measured mass spectrum (m/z) is a convolution of the gas content, sensitivity coefficient and fragmentation pattern coefficient of each component[116][117]. The ion current of the major peaks measured by QMS with CO₂ gas introduction is shown in Table 5.1. The rightest row in Table 5.1 is the candidate molecule. The inside of the parenthesis is the mother molecule. We assume O, C, CO, N, N₂ and CO₂ as the content. By analyzing the data with the pattern coefficient of QMS[116], the partial pressure of these molecules during the experiment can be extracted. For example, the peak at 44 is composed by CO₂ only. Because a part of CO₂ fragments into CO(m/z=28), O(m/z=16), and C(m/z=12), these components has to be accounted. The ion current by CO₂ is the total of these components as

$$I_{CO_2} = I_{44} + 0.0885I_{44} + 0.0805I_{44} + 0.058I_{44} = 5.90 \times 10^{-10}$$

0.0885 is the pattern coefficient of CO from CO₂ by QMS, and so on.

Because the peak at 28 contains not only CO, but also CO as the fragmentation component of CO₂ and N₂, the ion current of CO can be estimated by subtracting

these components from I_{28} as

$$I_{CO} = 1.04(I_{28} - I_{14}/(0.0790) - 0.0885I_{44}) = 1.87 \times 10^{-10}$$

N_2 contribution is extracted from the height of the peak at 14 which contains only N contribution. The factor 1.04 is the correction, because a part of CO fragments into C and atomic oxygen.

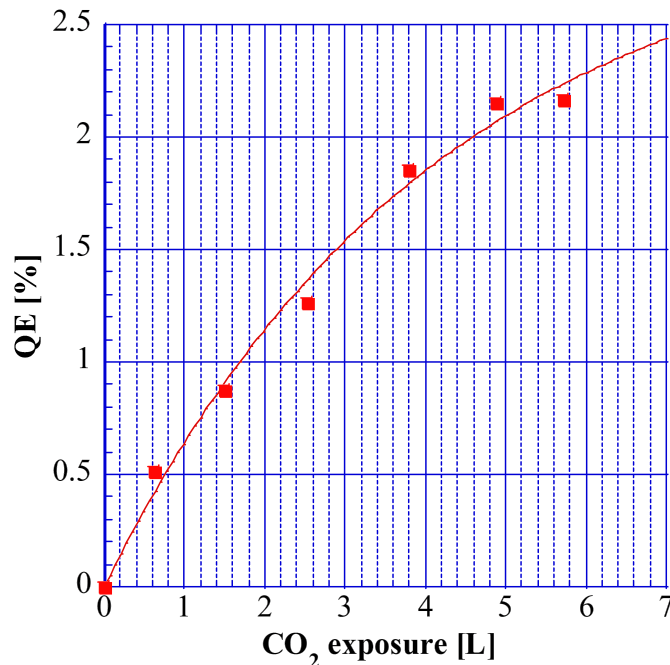


Figure 5.7: The height of each peak in Fig.5.3 is shown as a function of CO_2 gas exposure. The red solid line is a fitting curve by assuming Eq. (5.3).

The peak at 16 is composed not only by atomic oxygen, but also fragmentations as $O(CO_2)$ and $O(CO)$. Although the fragmentation components of CO_2 and CO can be estimated from the heights of these peaks at 44 and 28, respectively, but the peak at 28 contains contributions from $CO(CO_2)$ and N_2 as we discussed. We have to subtract these components from I_{28} . The ion current of atomic oxygen is estimated as

$$I_O = I_{16} - 0.0805I_{44} - 0.0102(I_{28} - I_{14}/(0.0790) - 0.0885I_{44}) = 0.49 \times 10^{-10}$$

From these ion currents, the partial pressure p for each molecule is obtained with

$$p = \frac{I}{\beta S}$$

where I is the ion current for each molecule, β is the sensitivity coefficient[117], and S is relative sensitivity to nitrogen. The fraction of CO₂, CO, and O during the experiment was estimated to be 0.75:0.18:0.07. μ is 0.39.

The ratio of CO₂, CO, and O is different from the natural ratio, because our system has an ionization vacuum gauge which stimulates CO₂ molecule. QMS was in operation only when QMS spectrum was measured and the period was short comparing to the experimental period. Then, the gas contains the fragment components by the ionization gauge, but the fragmentation by QMS occurred only in QMS spectrum measurement. The partial pressure ratio during the experiment (ionization gauge on, QMS off) was obtained by analyzing the QMS spectrum with the pattern coefficient of QMS ion source.

As same as that for CO₂ case, the content was estimated with the same manner, when O₂ gas was introduced. O₂ molecule composes peaks at 32 (O₂) and 16 (O) as the fragment product, but atomic oxygen composes only a peak at 16. The fraction of O₂ molecule and atomic oxygen during the experiment was estimated to be 0.75:0.25.

To determine both activation ability of the O₂ molecule and atomic oxygen independently, the NEA activations with CO₂ and O₂ gas were analyzed together. The expected evolution of the QE η for the activation with O₂ is

$$\eta = \alpha_1 x_1 + \alpha_2 x_2, \quad (5.4)$$

where α_2 is the activation ability of O₂ molecule and x_2 is the exposure of O₂ molecule.

Three parameters, α_1 , α_2 , and β can be determined with the data of activations with O₂ and CO₂. The results are shown in Figure 5.6 and 5.7 as the fitting curves. α_1 and α_2 (activation abilities of atomic oxygen and O₂ molecule) were estimated to be $7.7 \pm 0.1 \text{ L}^{-1}$ and $15.4 \pm 0.1 \text{ L}^{-1}$, respectively. The error of α_1 and α_2 are estimated by three measurements with CO₂. The center value is the average and the error was half of the peak-to-peak value. We found that O₂ molecule has an activation ability that is approximately twice of that of atomic oxygen. This fact can be explained as that the activation ability is simply proportional to the number of atomic oxygen provided to GaAs-Cs surface. The degradation ability β of CO was estimated to be $0.91 \pm 0.09 \text{ L}^{-1}$ which can be compared to 0.84 L^{-1} in Ref. [115]. These numbers are consistent to each other within the error. The error of β is estimated with the same manner for α .

Chapter 6

Summary

The accelerator has been a powerful tool to “accelerate” the scientific studies and applications. Especially, the ring accelerator (e+ e- ring collider and the third generation synchrotron light source) is playing an important role in the last 30 years in the high energy physics and synchrotron science discipline. On the other hand, the ring accelerator is reaching the performance limits in two contexts. One is the beam energy which is limited by huge energy loss by synchrotron radiation. Another is the beam emittance which is limited by equilibrium state of the stored beam. Many new accelerator projects based on Linac are proposed and constructed to break the limitations. In Linac, the particle source is taking a crucial role to determine the accelerator performance and the photo-cathode is the state of the art.

In this thesis, we studied a couple of subjects for the advanced photo-cathode. One is substrate dependence of CsK₂Sb cathode which is the best cathode for high brightness electron beam at this moment. Another is NEA GaAs activation with other gas species than O₂. NEA GaAs is the only solution for highly spin polarized electron source.

CsK₂Sb photo-cathode was fabricated on several substrates as the test sample. GaAs(100), Si(100), and Si(111) were examined. We found that the cleaned substrates resulted in higher performance than the as-received substrates for all materials. By comparing cathodes on GaAs(100), Si(100), Si(111), and Mo [25][29][31], we found that the cathode on GaAs(100), Si(100), and Mo(100) had significantly better performance than that on Si(111) and Mo(amorphous). It showed that the cathode performance depends strongly not only on the substrate material and surface state, but also on the crystallinity and the surface direction. This is the first experimental evidence for substrate surface direction dependence of CsK₂Sb photo-cathode performance. The difference can be explained that the band structure of CsK₂Sb. The result is significant showing importance of substrate choice

on material, crystallinity and surface direction. This fact has an impact on the experimental physics with accelerators, because there is some potential to improve a thin-film cathode performance by revisiting the substrate crystallinity and surface direction of the substrate. The high QE has a large merit to generate a high brightness electron beam by relaxing requirements for the drive laser. The fewer requirements for the laser make the system reliable, and stable. The availability of the system is improved and the effective cost of the project (cost per operation time) becomes less. Our result has a potential of the large impact on the accelerator science from this point of view.

We examined the NEA activation of GaAs cathode with O_2 , CO_2 , CO and N_2 to understand property of the NEA GaAs cathode. In a nominal activation with O_2 gas, we found that the height of each yo-yo peak are proportional to O_2 exposure. CO and N_2 did not activate the NEA GaAs cathode at all. CO_2 activated the NEA GaAs cathode, but the QE was 2.3% which was much lower than that with O_2 . We found that the activation ability of O_2 molecule and atomic oxygen were $15.4 \pm 0.1 \text{ L}^{-1}$ and $7.7 \pm 0.1 \text{ L}^{-1}$, respectively. The low QE of the cathode activated with CO_2 can be explained with the degradation by CO to the NEA surface. The degradation ability of CO was estimated to be $0.91 \pm 0.09 \text{ L}^{-1}$, which is consistent to 0.84 by a preceding study[115]. This effort is the first experiment to perform the NEA activation with CO_2 and the first measurement for the activation ability of O_2 and O , separately.

Although these experimental facts provide useful information for better understanding of the NEA surface, it is still not sufficient. Establishing a robust NEA GaAs cathode is a future issue.

References

- [1] Wolfgang K. H. Panofsky, Evolution of Particle Accelerators & Colliders (1997).
- [2] J. Beringer et al.: High-energy collider parameters. Phys. Rev. D. Vol. 86, Nr. 1, 010001, 2012, S. 317-321.
- [3] Web[<https://en.wikipedia.org/wiki/SPEAR>].
- [4] Web[http://argus-fest.desy.de/e301/e303/ARGUS_SchopperFestschr_1.Blocksatz.pdf].
- [5] Yoshitaka Kimura, Proc. of the 2nd European Particle Accelerator Conference. Nizza, Frankreich, 12-16. Juni 1990, S. 23-27.
- [6] "The LEP Collider, from design to approval and commissioning" CERN 1990 historical reference with much information on the design issues and details of LEP
- [7] M.G. Billing et al., 2016 JINST **11** T10009.
- [8] Shou-Xian Fang, Sen-Yu Chen, Particle Accelerators. Vol. 25, 1990, S. 51-61.
- [9] J. R. Rees, SLAC-PUB-1911, PEP-243, March 1977, (A).
- [10] Levine, I.; TOPAZ Collaboration (1997). "Measurement of the Electromagnetic Coupling at Large Momentum Transfer". Physical Review Letters. 78 (3): 424-427.
- [11] JOHN T. SEEMAN SLAC-PUB-5748 June 1992 (A).
- [12] T. Behnke *et al.*, International Linear Collider Technical Design Report, KEK Report 2013-1(2013).
- [13] "A Brief History of the NSLS". BNL.gov. Retrieved August 4, 2010.
- [14] Web[https://en.wikipedia.org/wiki/BESSY#cite_note-1].

- [15] Web[<http://www2.kek.jp/imss/pf/eng/>].
- [16] nature.com 29 March 2016, 24 hours at the X-ray factory.
- [17] "X-Ray Storage Ring". BNL.gov. Retrieved August 4, 2010.
- [18] T. Hotta (27 October 2009). "Laser Electron Photon Experiment at SPring-8". Osaka University. Retrieved 2009-11-21.
- [19] Einfeld, Dieter (2014-11-02). "Multi-bend Achromat Lattices for Storage Ring Light Sources". *Synchrotron Radiation News*. 27 (6): 4-7.
- [20] Textbook of accelerator physics, Graduate School for Advanced Sciences of Matters, Hiroshima University.
- [21] ERL Conceptual Design Report, KEK Report 2012-4 (2012).
- [22] Georg H. Hoffstaetter, Sol M. Gruner and Maury Tigner *et al.*, Cornell Energy Recovery Linac Science Case and Project Definition Design Report, Cornell University (2013.6).
- [23] M. Altarelli *et al.*, The European X-ray Free Electron Laser Technica Design Report, DESY 2006-97 (2006).
- [24] E. Chevallay, J. Durand, S. Hutchins, G. Suberlucq and M. Wurgel, *Nucl. Instrum. Methods Phys. A***340**, 146 (1994).
- [25] M. A. Nichols, Research Experiences for Undergraduates (REU) Report, 2011, Cornell University. (available at: www.lepp.cornell.edu/ib38/reu/11/Nichols_report.pdf (2011)).
- [26] S. Karkare, I. V. Bazarov, L. E. Boulet, M. Brown, L. Cultrera, B. Dunham, N. Erickson, G. Denham, A. Kim, B. Lillard, T. P. Moore, C. Nguyen, W. Schaff, K. W. Smolenski and H. Wang, Proceedings of IPAC 2013, Pasadena, CA, TUOAB1 (2013).
- [27] L. Cultrera, I. V. Bazarov, J. V. Conway, B. Dunham, S. Karkare, Y. Li, X. Liu, J. M. Maxson and K. W. Smolenski , Proceedings of 2011 Particle Accelerator Conference, New York, NY, WEP244 (2011).
- [28] John N. Galayda "LCLS-II Project" Proceedings of IPAC2014, Dresden, Germany (2014).

- [29] A. Burrill, I. Ben-Zvi, T. Rao, D. Pate, Z. Segalov, D. Dowell, 21st IEEE Particle Accelerator Conference, Knoxville, TN, USA, 16 - 20 May 2005, pp.2672.
- [30] M. Kuriki, A Yokota, K. Negishi, R. Kaku, M. Urano, Proceedings of IPAC2016, Busan, Korea (2016).
- [31] Valeri. S, Lancellotti. M. G, Mariani. C, Di Bona. A, Michelato. P, Pagani. C, Sancrotti. M, 4th European Particle Accelerator Conference, London, UK, 27 Jun-1 Jul 1994, pp.1459.
- [32] D. T. Pierce, F. Meier and P. Zurcher, Appl. Phys. Lett. **26**, 670 (1975).
- [33] D. T. Pierce, R. J. Celotta, G.- C. Wang, W. N. Unertl, A. Galejs, C. E. Kuyatt and S. R. Mielczarek, Rev. Sci. Instrum. **51**, 478 (1980).
- [34] Tigner, Maury (1965). "A Possible Apparatus for Electron Clashing-Beam Experiments". Nuovo Cimento. 37: 12281231.
- [35] Web[<https://www.classe.cornell.edu/Research/ERL/ErlIntroduction.html>]
- [36] Sol M. Gruner, Don Bilderback, Ivan Bazarov, Ken Finkelstein, Geoffrey Krafft, Lia Merminga, Hasan Padamsee, Qun Shen, Charles Sinclair and Maury Tigner, Rev. Sci. Instrum. **73**, 1402 (2002).
- [37] S. Fukuda *et al.*, Proceedings of IPAC'10, Kyoto, Japan, THPEB046 (2010).
- [38] web[http://www.spring8.or.jp/ja/about_us/whats_sp8/facilities/accelerators/storage_ring/]
- [39] Huang, Z.; Kim, K. J. (2007). "Review of x-ray free-electron laser theory". Physical Review Special Topics - Accelerators and Beams. 10 (3). Bibcode:2007PhRvS..10c4801H. doi:10.1103/PhysRevSTAB.10.034801.
- [40] "Southeastern Universities Research Association Thomas Jefferson National Accelerator Facility". Retrieved 2015-11-19.
- [41] "XFEL information webpages". Retrieved 2007-12-21.
- [42] https://en.wikipedia.org/wiki/Free-electron_laser.
- [43] https://www-ssrl.slac.stanford.edu/lcls/lcls_parms.html.
- [44] (LCLS-II Design Study Group), SLAC Report No. LCLSII-1.1-DR-0001-R0, 2014.

- [45] "ILC - Status of the project". www.linearcollider.org. Retrieved 2016-12-14.
- [46] Ties Behnke *et al.*, ILC Technical Design Report Volume 1 - Executive Summary (2013).
- [47] <https://arstechnica.com/science/2013/06/the-international-linear-collider-will-be-a-higgs-factory/>
- [48] LHC Design Report Volume I : The LHC Main Ring Web[<http://ab-div.web.cern.ch/ab-div/Publications/LHC-DesignReport.html>].
- [49] <http://legacy.kek.jp/ja/activity/accl/ILC.html>
- [50] " ILC Reference Design Report ", ILC-Report-2007-1, 2007.
- [51] Ivan V. Bazarov *et al.*, J. Appl. Phys. **103**, 054901 (2008).
- [52] P. G. O'Shea, Nucl. Instrum. Methods Phys. A **358**, 36 (1995).
- [53] T. Srinivasan-Rao, J. Fischer and T. Tsang, J. Appl. Phys. **69**, 3291 (1991).
- [54] Ajay K. Pandey, Paul E. Shaw, Ifor D. W. Samuel and Jean-Michel Nunzi, Appl. Phys. Lett. **94**, 103303 (2009).
- [55] Y. Aoki *et al.*, Proceedings of the 1999 Particle Accelerator Conference, New York, pp. 2018-2020 (1999).
- [56] Schmerge, J.F *et al.*, SLAC-PUB-10763, LCLS-TN-04-13.
- [57] M.,Yoshimurra and Y. Mori, J. Plasma Fusion Res. **85**, 239 (2009).
- [58] C. Ghosh and B. P. Varma J. Appl. Phys., Vol. 49, No.8, August (1978).
- [59] A.H. Sommer Photoemissive Materials: Preparation, Properties and Uses (1968).
- [60] Web[https://www.hamamatsu.com/resources/pdf/etd/PMT_TPMZ0002E.pdf].
- [61] D. H. Dowell, S. Z. Bethel, and K. D. Friddell, Nucl. Instrum. Methods Phys. Res., Sect. A **356**, 167 (1995).
- [62] F. Sannibale, B. Bailey, K. Baptiste, A. Catalano, D. Colomb, J. Corlett, S. De Santis, L. Doolittle, J. Feng, D. Filippetto, G. Huang, R. Kraft, D. Li, M. Messerly, H. Padmore, C. F. Papadopoulos, G. Portmann, M. Prantil, S. Prestemon, J. Qiang, J. Staples, M. Stuart, T. Vecchione, R. Wells, M. Yoon,

and M. Zolotarev, “Status of the LBNL normal-conducting CW VHF electron photo-gun,” in Proceedings of the 2010 Free Electron Laser Conference, Malmo, Sweden, August (2010).

- [63] L. Kalarasse *et al.*, J. Phys. Chem. Solids **71**, 314 (2010).
- [64] R. W. G. Wyckoff, *Crystal Structures* (Wiley, New York, 1960), Vol. 2.
- [65] A. R. H. F. Ettema *et al.*, Phys. Rev. B **66**, 115102 (2002).
- [66] W. H. McCarroll, J. Phys. Chem. Solids **26**, 191 (1965).
- [67] L. Guo, *et al.*, PTEP, 2017, 033G01.
- [68] M. A. A. Mamun, A. A. Elmustafa, C. Hernandez-Garcia, R. Mammei and M. Poelker, J. Vac. Sci. Technol. A **34**, 021509 (2016).
- [69] Bruce Dunham *et al.*,. Appl. Phys. Lett. 102, 034105, 2013.
- [70] I.V. Bazarov, et al. Appl. Phys. Lett. **98**, 224101 (2011).
- [71] A. V. Lyashenko *et al.*, Journal of Instrumentation, Volume **4**, (July 2009).
- [72] J. Smedley, T. Rao and E. Wang, AIP Conf. Proc. **1149**, 18th Int’l. Spin Physics Symp., pp.1062-1066(2009).
- [73] S. Schubert, J. Smedley, T. Rao, M. Ruiz-Oses, X. Liang, I. Ben-Zvi, H. Padmore and T. Vecchione, Proceedings of IPAC2013, Shanghai, China, MOPFI005 (2013).
- [74] M. Ruiz-Oses et al., APL Materials **2**, 121101 (2014)
- [75] S. Schubert et al., Journal of Applied Physics **120**, 035303 (2016).
- [76] J.J. Scheer, J. van Laar, Solid State Commun. 3 (1965) 189.
- [77] J.J. Scheer, J. van Laar, Solid State Commun. 3 (1965) 189.
- [78] J.E. Clendenin *et al.*, AIP Conf.Proc. **675** (2003) 1042-1046.
- [79] D. Schultz, *et al.*, Stanford Linear Accelerator Center, SLAC Pub 6606, (1994).
- [80] Hendrik Bluhm, *et al.*, Nature Physics **7**, 109113 (2011)

- [81] Jie Pan "Towards a Precision Measurement of Parity-Violating e-p Elastic Scattering at Low Momentum Transfer" Department of Physics and Astronomy University of Manitoba Winnipeg (2012).
- [82] Web[<http://www-sldnt.slac.stanford.edu/alr/slc.htm>].
- [83] YIMEI ZHU "MODERN TECHNIQUES FOR CHARACTERIZING MAGNETIC MATERIALS" KLUWER ACADEMIC PUBLISHERS. CHAPTER 9. (2005).
- [84] Tang, H, *et al.*, In *Koeln 1995, Proceedings, Polarized beams and polarized gas targets* SLAC-PUB-6918, C95-06-06.1
- [85] X. Jin *et al.*, Appl. Phys. Express **1**, 045002 (2008).
- [86] A. Moy *et al.*, AIP Conf. Proc. **1149** 1038 (2009).
- [87] C. Y. Su, W. E. Spicer, and I. Lindau, J.Appl. Phys., **54**, pp. 1413-1422 (1983).
- [88] K. Togawa *et al.*, Nucl. Instr. And Meth. A, **414**, pp.431-445 (1998).
- [89] Zhi Liu *et al.*, Appl. Phys. Lett. **92**, 241107 (2008)
- [90] O. E Tereshchenko, S. I Chikichev and A. S Terekhov, Appl. Surf. Sci. **142**, 75 (1999).
- [91] T. Yamada, J. Fujii, and T. Mizoguchi, Surf. Science **479** (2001) 33-42.
- [92] Y. Masumoto, Graduate School of Advanced Sciences of Matter. Master Thesis. (2012)
- [93] K. Tsubota *et al.*, Journal of Physics: Conference Series **430** (2013) 012079.
- [94] Atsushi Era *et al.*, Journal of Physics: Conference Series **298** (2011) 012012.
- [95] D. Durek *et al.*, Appl. Surf. Sci. **143**, 319 (1999).
- [96] Tatsuaki Wada *et al.*, Japanese Journal of Applied Physics, Volume 29, Part 1, Number 10.
- [97] M. Kurik *et al.*, Proceedings of IPAC2013, Shanghai, China, MOPFI012.
- [98] J. Grames *et al.*, AIP Conf. Proc. **980**, 110 (2008).
- [99] M. Kuriki *et al.*, Proceedings of IPAC2013, Shanghai, China, MOPFI014.

- [100] Konomi, Taro *et al.*, Proceedings of the 5th annual meeting of Particle Accelerator Society of Japan and the 33rd Linear Accelerator Meeting in Japan.
- [101] Bruce Dunham *et al.*, Appl. Phys. Lett. 102, 034105 (2013).
- [102] Web[https://www.ulvac.co.jp/products_e/components/vacuum-pump/ion-pump/acter-pumpspst-100cx100ax].
- [103] Web[<https://www.saesgetters.com/sites/default/files/CapaciTorr%20Products%20Datasheets.pdf>].
- [104] Web[https://www.saesgetters.com/sites/default/files/AMD%20Brochure_0.pdf].
- [105] S. Valeri *et al.*, 4th European Particle Accelerator Conference, London, UK, 1459 (1994).
- [106] Karen Reinhardt, Werner Kern, Handbook of Silicon Wafer Cleaning Technology 9.2.2 William Andrew; 2 edition (2008/1/24).
- [107] T. Miura *et al.*, J. Appl. Phys. **79** (8), 15 4373 (April.1996).
- [108] W. Shin, H. Cho, H. Lee and H. Jeong, J. Korean Phys. Soc. **54**, 1077 (2009).
- [109] C. Logofatu, C. C. Negri, R. V. Ghita, F. Ungureanu, C. Cotirlan, C. G. A. S. Manea and M. F. Lazarescu in *Crystalline Silicon - Properties and Uses*, (InTech, 2011) Chap. 2.
- [110] K. Kutsuki, T. Ono and K. Hirose, Sci. Tech. Adv. Mater. **8**, 204 (2007).
- [111] C. Kittel, *Introduction to Solid State Physics* (Wiley, 2004), 8th ed.
- [112] C. Shonaka, et al., Proceedings of Particle Accelerator Conference (PAC09), MO6RFP069, 2009.
- [113] D.T. Pierce, et al., Rev. Sci. Instr. **51** (1980) 478.
- [114] Zou J, Chang B, Yang Z, Qiao J and Zeng Y 2008 Appl. Phys. Lett. **92** 172102.
- [115] N Chanlek *et al.*, J. Phys. D: Appl. Phys. **47** (2014) 055110.
- [116] K. Fuwa "Quadrupole mass spectrometer - principle and application (1977)", Kodansha, (1977), pp50-51.
- [117] K. Uchida, Graduation thesis Graduate School of Advanced Sciences of Matter, Hiroshima University. (2012).

Appendix A

NEA GaAs as a polarized electron source

Polarized electrons are obtained by irradiating laser light circularly polarized (Ti:Sa wavelength 700 to 800 nm) into a semiconductor GaAs crystal and extracting electrons generated by the photoelectric effect with a DC electric field. Figure A.1 (a) shows the band structure of bulk GaAs crystal. The GaAs crystal has a charged zone with an angular momentum of $3/2$ in the outermost shell. Valence electrons are excited by photons corresponding to the energy difference between this band and the conduction band, and taken out. Free electrons in the conduction band can only take state of helicity ± 1 , so if the photon is circularly polarized, the transition becomes selective from the law of conservation of angular momentum. Let's assume excitation by right-handed photons. The transition indicated by the solid line in Figure A.1 (a) is due to the right-handed photon. Since the transition from the level of $J = 1/2$ is strongly suppressed when the energy of the photon is set to 1.43 eV or more and less than 1.77 eV, only transition from $m = -3/2, -1/2$ state of $J = 3/2$ is possible. The state density of $J = 3/2$ level is 3: 1 for $m = -3/2$ and $m = -1/2$ by ClebschGordan coefficient. Therefore, 75% of electrons obtained in the conduction band are $m = -1/2$, and 25% are $m = +1/2$ state. The polarization degree of the beam is

$$P = \frac{N_+ - N_-}{N_+ + N_-} \quad (\text{A.1})$$

Where N_{\pm} is the density of the electron's helicity state. Therefore, the degree of polarization of electrons is 50% by irradiation of polarized photon. The polarization degree of the electron beam is determined by the density of the $J = 3/2$ state which is the composite state of the spin-orbital angular momentum. This is impossible to change, because it is decided by quantum mechanics. Therefore,

50% polarization is the theoretical limit value and it is impossible to exceed this as long as bulk GaAs is used.

A polarization degree exceeding 50% was obtained by breaking the symmetry of the GaAs crystal and solving the degeneracy of the $J = 3/2$ state. Two methods as a strained thin film and a superlattice thin film by SLAC and Nagoya University were developed as a method to solve the degeneracy. Figure A.1 (b) shows that the band structure of the GaAs crystal in a state where the degeneracy is resolved. An energy gap is generated between $m = \pm 3/2$ and $m = \pm 1/2$ at $J = 3/2$ due to the degeneracy being resolved. The transition from the $m = \pm 1/2$ state can be suppressed by adjusting the energy of the photon. In principle, a degree of polarization of 100% is possible, and polarizations of around 90% are also obtained in actual beams[85].

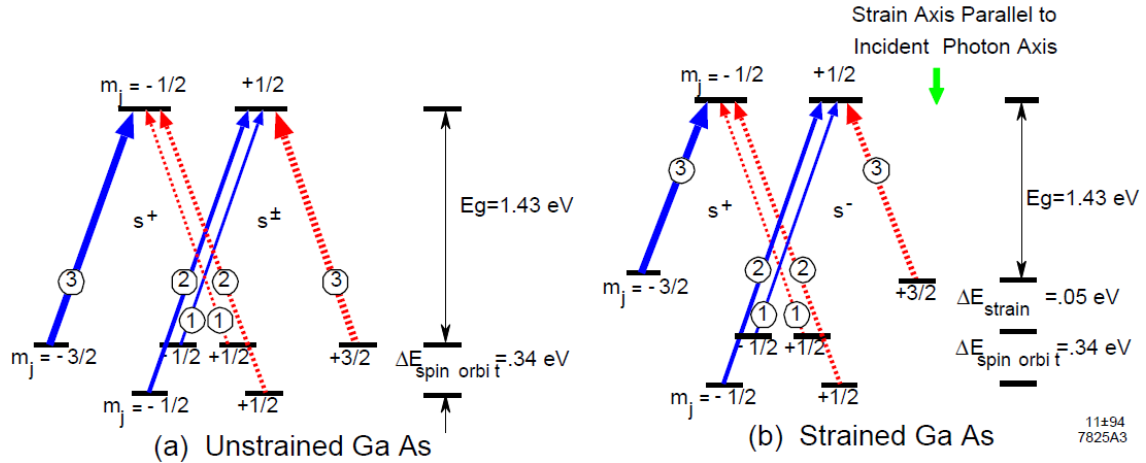


Figure A.1: The band structure of GaAs and the state of excitation by photons to the conduction band. (a) shows bulk GaAs crystal, (b) is a diagram of distorted GaAs crystal. Degeneracy of angular momentum 3/2 state is solved by distortion.[20]

Appendix B

Atomic arrangement model of unit cell

In chapter 4, we explained that the growth direction is different depending by the atomic arrangement between the CsK_2Sb and the substrate. We explain in detail here with atomic arrangement model of unit cell.

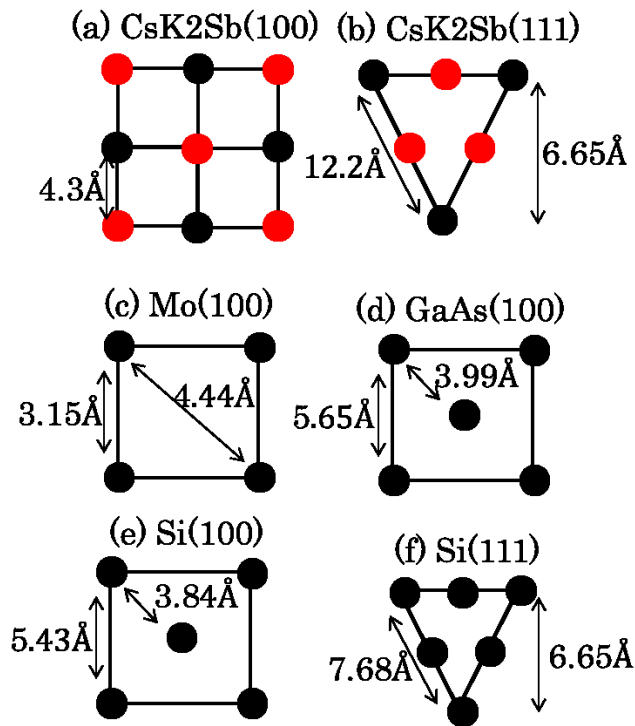


Figure B.1: Atomic arrangement of $\text{CsK}_2\text{Sb}(100)$ and $\text{CsK}_2\text{Sb}(111)$ on the $\text{Mo}(100)$, $\text{GaAs}(100)$, $\text{Si}(100)$, and $\text{Si}(111)$ surfaces. The lattice constants of Mo , Si , and GaAs are 3.15 Å, 5.43 Å, and 5.65 Å, respectively [111].

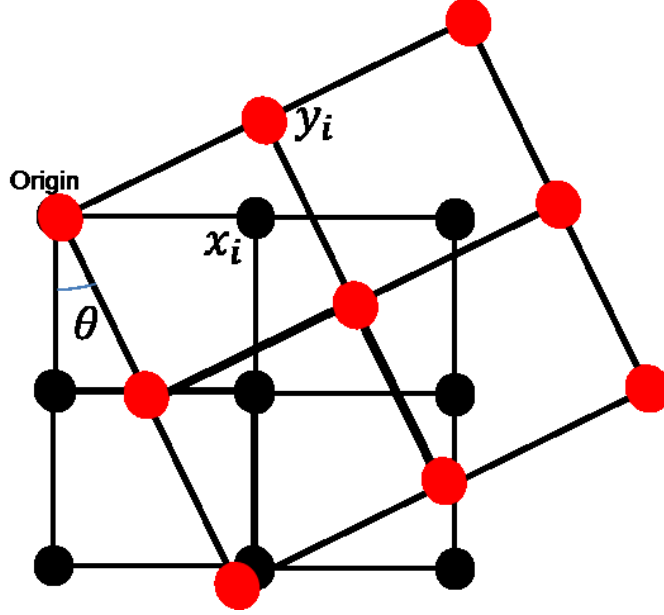


Figure B.2: ζ is obtained with the atomic positions of the substrate and CsK₂Sb by Eq. B.1. By rotating angle θ , we take the minimum value as a representative matching index.

Figure B.1 shows that the surface atomic arrangements of CsK₂Sb(100), CsK₂Sb(111), Mo(100), GaAs(100), Si(100), and Si(111) surfaces. To examine the atomic arrangement matching, we introduce the matching index ζ as

$$\zeta(hkl) = \frac{1}{n-1} \sum_{i=1}^n \frac{(x_i - y_i)^2}{x_i^2} \quad (\text{B.1})$$

where hkl are the Miller indices defining the plane of the CsK₂Sb crystal, n is the number of atoms used to evaluate the matching, and \vec{x}_i and \vec{y}_i are the atomic position vectors for CsK₂Sb and the substrate, respectively. Figure B.2 shows the schematic calculation of the matching index. One atom of the substrate and CsK₂Sb overlap at the origin, which is why the index is divided by $n-1$. Moreover, ζ is proportional to the square of the displacement between each atom of CsK₂Sb and the nearest atom in the substrate, normalized by the distance of the atom from the origin. The red and blue solid circles represent the atoms of substrate and CsK₂Sb, respectively. The rotation angle θ is a degree of freedom on ζ , as shown in Figure B.2. We take the minimum value as a representative ζ by rotating the angle.

Therefore, we calculated ζ for several surface directions of the CsK₂Sb crystal. Figure B.3, Figure B.4 and Figure B.5 show $\zeta(100)$, $\zeta(110)$ and $\zeta(111)$ for Mo(100), GaAs(100), Si(100), and Si(111). Each ζ value is plotted as a function of the

Table B.1: The maximum QE of the CsK₂Sb photo-cathode with ζ of CsK₂Sb(100) and CsK₂Sb(111) surface at 532 nm are summarized.

Substrate	ζ (100)	ζ (110)	ζ (111)	QE[%]@532nm
cleaned Mo(100)	1.3e-3	1.5e-2	1.0e-2	10.0[25]
cleaned GaAs(100)	5.0e-3	2.4e-2	4.4e-2	10.0 \pm 0.2
as-received GaAs(100)	-	-	-	5.5 \pm 0.2
cleaned Si(100)	1.1e-2	2.0e-2	3.5e-2	9.4 \pm 0.7
as-received Si(100)	-	-	-	4.8 \pm 0.6
cleaned Si(111)	3.5e-2	7.2e-3	6.0e-3	2.3 \pm 0.3
as-recieved Si(111)	-	-	-	1.6 \pm 0.1

rotation angle θ . For $\zeta(100)$, the rotation angle of $\pi/4$ gives the representative value for Mo(100), GaAs(100), Si(100), and Si(111). For $\zeta(110)$, the representative values for Mo(100), GaAs(100), Si(100) and Si(111) were given at the angles of 0, $\pi/4$, $\pi/4$, and $\pi/6$, respectively. For $\zeta(111)$, the representative values for Mo(100), GaAs(100), Si(100) and Si(111) were given at the angles of $\pi/6$, $\pi/12$, $\pi/12$, and $\pi/6$, respectively. The matching between CsK₂Sb(100) and Si(100), Mo(100) or GaAs(100) is best. The matching between CsK₂Sb(111) and Si(111) is best.

The results are summarized in Table B.1. Two facts are obvious from these results.

- The QE of the cleaned substrate is almost twice that of the as-received substrate for all materials.
- The QE of Mo(100), GaAs(100), and Si(100) showed a similar value of $QE \sim 10\%$ for the cleaned substrate. On the other hand, Si(111) showed a lower QE value than the other substrates.

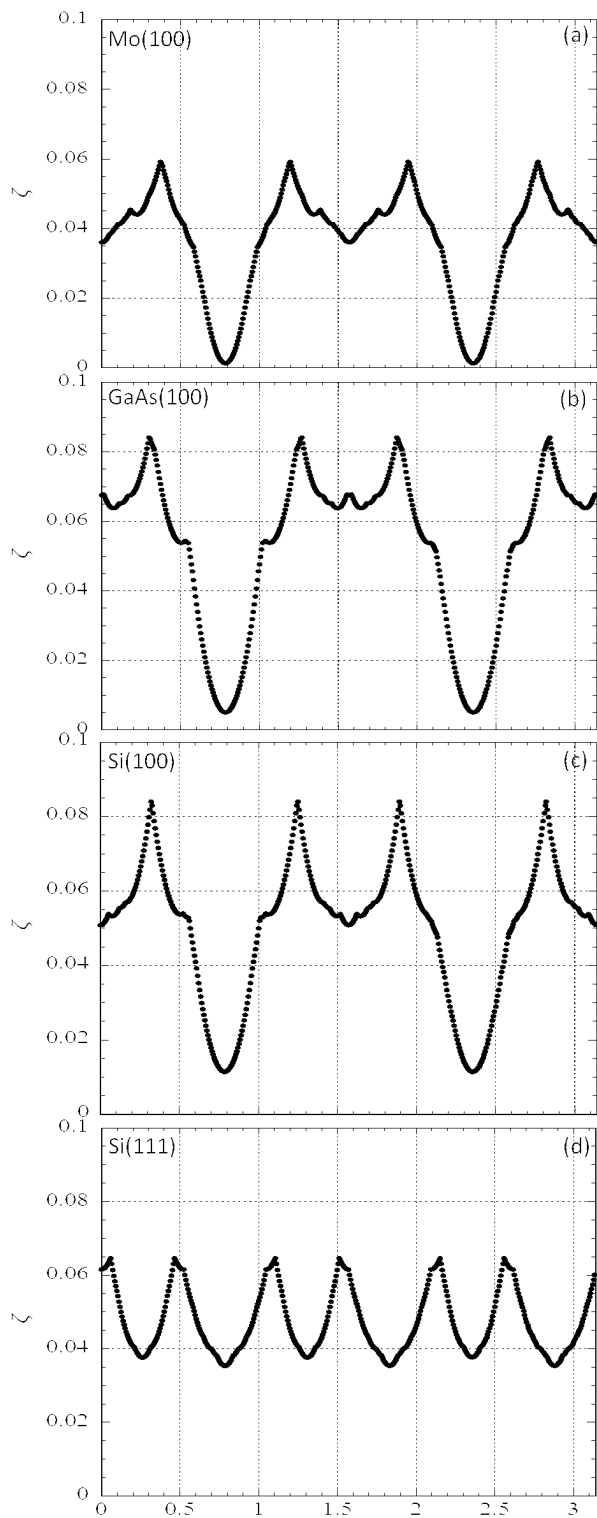


Figure B.3: $\zeta(100)$ is calculated as a function of the rotation angle θ for $\text{CSK}_2\text{Sb}(100)$ and the various substrates.

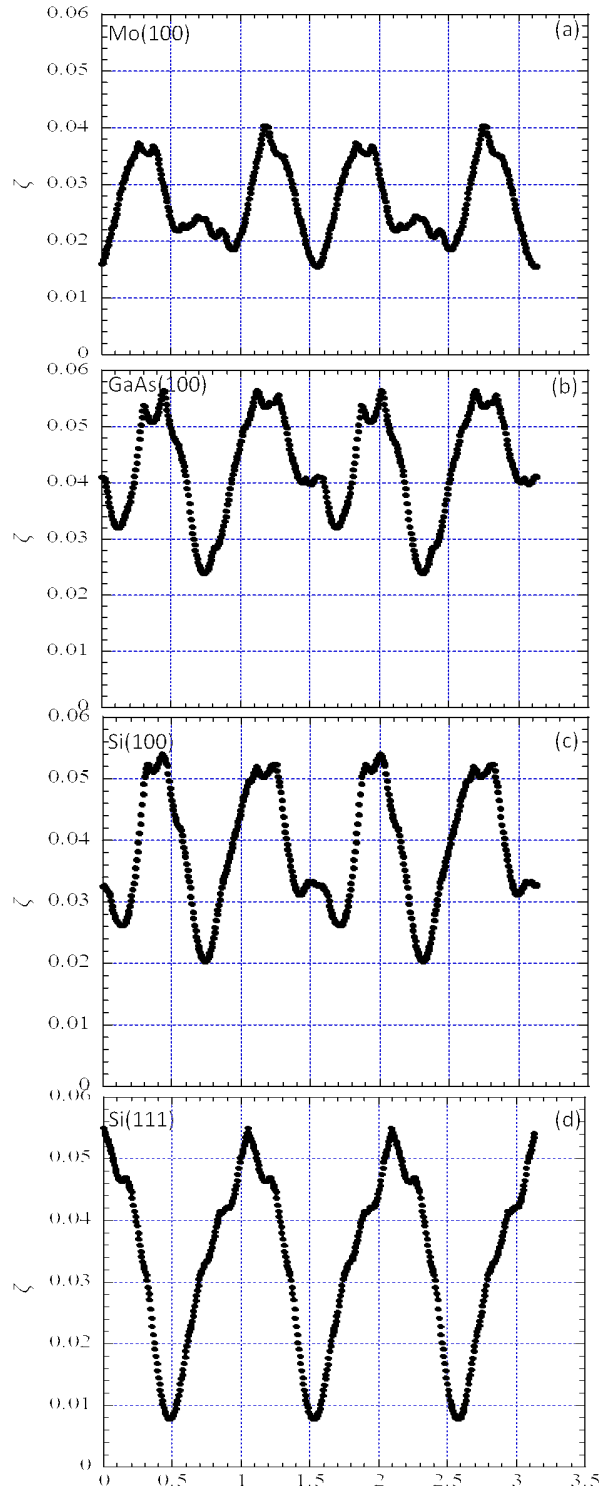


Figure B.4: $\zeta(110)$ is calculated as a function of the rotation angle θ for $\text{CSK}_2\text{Sb}(110)$ and the various substrates.

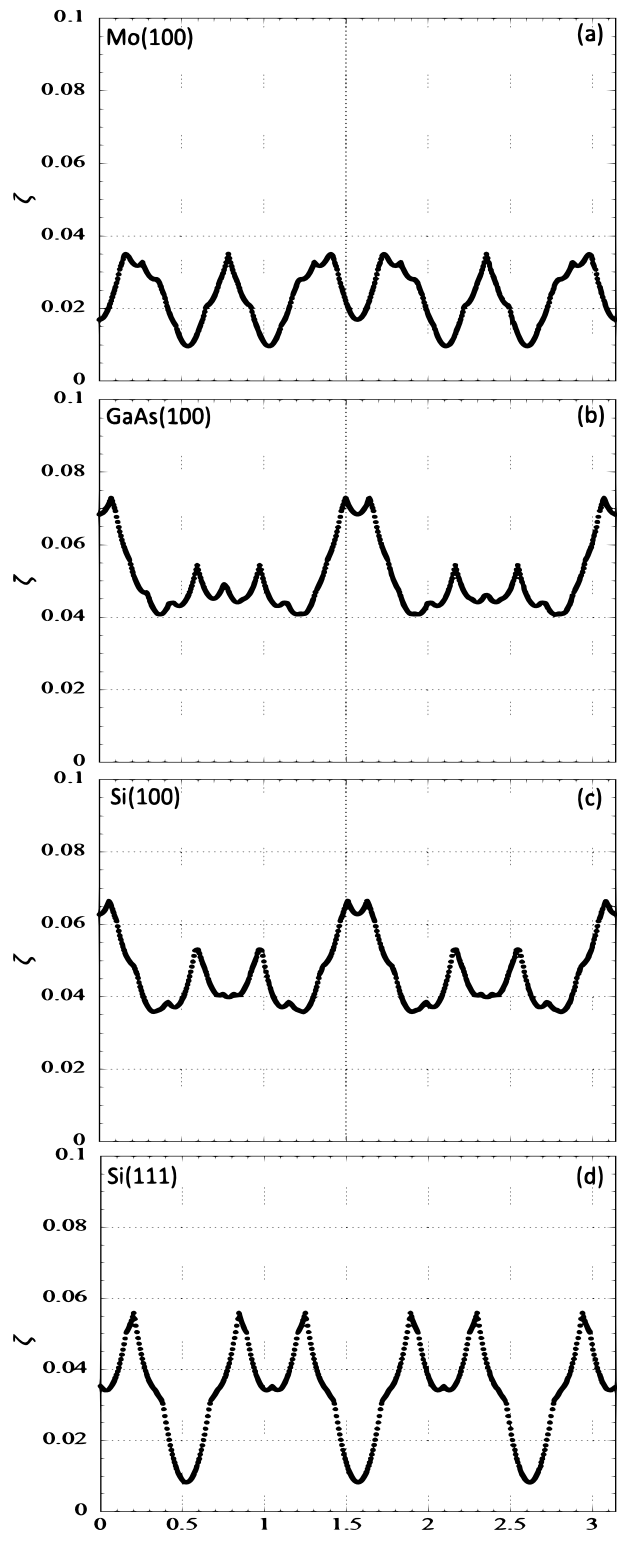


Figure B.5: $\zeta(111)$ is calculated as a function of the rotation angle θ for $\text{CSK}_2\text{Sb}(111)$ and the various substrates.